University of Trento

Department of Physics

BACHELOR THESIS

Heralded single photon sources based on intermodal four wave mixing

Advisor:
prof. Lorenzo Pavesi

Co-advisor:
dr. Stefano Signorini

Candidate:
Luca Garbi

Academic Year 2019/2020

Contents

Introduction

Integrated single photon sources are key building blocks for on-chip quantum computation, quantum information and quantum technologies in general. Single photon states can be produced through a heralding process between correlated photon pairs generated via nonlinear optical processes. On-chip heralded single photon sources based on spontaneous four wave mixing have been already demonstrated. The purpose of this thesis is to show the advantages and potentialities of intermodal four wave mixing in the single photon generation framework. The photon source is developed on a silicon chip, the ideal platform for integrated nonlinear processes and scalable quantum devices, thanks also to its mature and cheap fabrication technology. A heralded single photon source based on a IFWM process in silicon waveguides is here demonstrated.
In the first chapter the basics of the formation and propagation of waveguide modes are given, with a focus on optical multimode waveguides. Nonlinear optics is then introduced with a concise overview of the main second and third order nonlinear processes. A particular attention is paid to spontaneous four wave mixing and its inefficiencies in view of a single photon source application. Through this process, in fact, the signal and idler photons are generated close to the wavelength of the pump, thus limiting the generation spectrum. Moreover, narrow spectral post filtering is used to increase the spectral purity, limiting the brightness and the integration of these type of sources. Intermodal four wave mixing can be used to remove the need of tight spectral filtering and to achieve broad band quantum light generation, from the near to the mid infrared.
The second chapter initially introduce some elements of photon statistics and deals with the basics of probabilistic single photon sources. A close attention is paid to heralded single photon sources and the experimental metrics necessary in order to characterize their performance. The last part of chapter 2 presents a heralded single photon source based on intermodal FWM on a SOI multimode waveguide. A description of the chip used, which has been fabricated by the Centre for Materials and Microsystems of Bruno Kessler Foundation (Trento, Italy), is initially provided. Next, the experimental set-up for the source characterization is described. The measurements have been carried out by dr. Stefano Signorini and Matteo Sanna (master student) in the Nanoscience Laboratory, in the Department of Physics of the University of Trento.

The analysis I carried out on the measurements is presented in the last chapter of this thesis. The experimental demonstration of a silicon integrated source of heralded single photons is reported. The source exploits the intermodal four wave mixing to generate the heralding idler in the near infrared and the heralded signal in the mid infrared.

Chapter 1

Intermodal four wave mixing

In the first part of this chapter are laid the theoretical foundations of multimode photonics in optical waveguides. In particular it is discussed the formation of waveguide modes and the subsequent propagation and light coupling in multimode waveguides.
In the second part, after a brief introduction on nonlinear optical processes, four wave mixing in silicon waveguides will be presented. After a focus on the phase matching, intermodal four wave mixing is discussed.

1.1 Multimode photonics in optical waveguides

An optical waveguide is a physical structure that guides electromagnetic waves in the optical spectrum along a certain path. Optical waveguides are used as components in integrated optical circuits as "optical wires", thus yielding an analogy with the electrical wires of the well developed microelectronics. In the advancement of the latter, silicon has covered a central role for the last fifty years, making accessible to a wide public low cost and high speed communication. However, notwithstanding the increasing demand of data bandwidth and higher operation frequency, nowadays microelectronics is facing a physical limit in terms of minimum implementation size and performance. Stronger parasitic effects in the metallic connections occur at higher bandwidth, thus providing excessive power dissipation and signal losses. In order to overcome this limit, a viable solution is to change the information carrier: photons instead of electrons. Integrated photonics with silicon has been proved to be a very valuable approach for this purpose in the telecommunication band [1]. Moreover silicon photonics can rely on years of microelectronics research, exploiting its mass integration and cheap fabrication. In fact the cutting-hedge silicon-on-insulator (SOI) wafer technology happens to be the paradigm for micro-fabrication of silicon optical waveguides [2].

1.1.1 Formation of waveguide modes

The basic structure of a dielectric waveguide consists of a longitudinally extended high-refractive index n_2 optical medium, called the core, which is transversely surrounded by lower index media (n_1 and n_3), called cladding and substrate. The aforementioned success of silicon for the fabrication of waveguides is also related to its dioxide (Silica) that, with its low refractive index (~ 1.45 at $1.55\,\mu$m wavelength), is used as the cladding, surrounding the silicon core at a higher refractive index (~ 3.48 at $1.55\,\mu$m).
A guided optical wave propagates in the waveguide along its longitudinal direction thanks to this refractive index contrast. In fact the light is confined due to the total internal reflection at the borders of the core region, propagating through the waveguide. Therefore the waveguide is naturally associated with a critical angle θ_c so that all the waveguide modes propagating with an angle lower than the critical one will be confined, while the others will be radiated outside the core region.

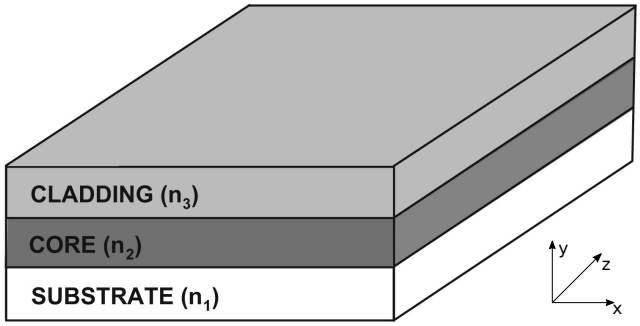

Figure 1.1: Planar waveguide, 3D representation with reference frame. Reprinted from [3].

A waveguide, depending on its core area, can support one or more modes, where the mode is a solution of the Maxwell equations for the specific waveguide geometry. Each mode has a correspondence with a spatial distribution of optical energy, whose lineshape does not change along the waveguide.
Instead of solving the Maxwell PDEs it is possible to evaluate the Helmoltz equation, i.e. the eigenvalue problem for the Laplace operator, that using the reference frame in Fig. 1.1, can be written as

$$(\nabla^2_{xy} + \beta_m)\mathscr{E}_m(x,y) = \frac{\omega^2}{c^2} n^2(x,y)\mathscr{E}_m(x,y), \qquad m = 1,2,\ldots, \tag{1.1}$$

where β_m is the propagation constant of the m-th waveguide mode, ω the frequency of the wave, $n(x,y)$ represents the spatial distribution of the refractive index and ultimately $\mathscr{E}_m(x,y)$ is the electric field profile.
For a single mode, the field intensity decreases while propagating along the waveguide and can be written as

$$\mathbf{E}_m(\mathbf{r},\omega) = \boldsymbol{\mathscr{E}}_m(x,y)e^{-\alpha_m z}, \qquad \text{where } \alpha_m = 2\,\mathrm{Im}(\beta_m), \tag{1.2}$$

is the attenuation coefficient. It is useful to rewrite

$$\beta_m = \frac{\omega}{v} = \frac{\omega}{c} n_m^{\text{eff}}, \tag{1.3}$$

where v is the phase velocity of the propagating wave and c is the speed velocity in vacuum. The last factor, n_m^{eff}, is an effective refractive index whose real part is just n and gives information on the phase acquired by the wave in its propagation, while the imaginary one is proportional to the losses through the waveguide.
Of course n_m^{eff} varies for different modes depending on the geometry of the waveguide and electric field polarization. Given a symmetric optical waveguide, i.e. with the same composition for cladding and substrate, it can be shown that the number of supported light modes is well approximated by [4]

$$N_{modes} = \frac{4}{\pi} \frac{w \cdot h}{\lambda^2} (NA)^2, \qquad NA = \sqrt{n_{core}^2 - n_{clad}^2} \tag{1.4}$$

where NA stands for *numerical aperture* and w, h are the width and height of the waveguide respectively. A major distinction for modes is given by the light polarization, that can be transverse electric (TE), i.e. with the dominant electric field component along the x direction, or transverse magnetic (TM), so with the dominant electric field along the y direction. Typically in integrated photonics the geometry of the waveguide are of the type $h < w$, that implies a more substantial confinement of TE modes with respect to TM.

1.1.2 Light propagation in multimode waveguides

Wavelength, polarization, waveguide geometry, core and cladding materials are all parameters that influence the effective refractive index of the optical modes. In the case of micronsize structures n_m^{eff} is largely dominated by the geometric dispersion rather than by the chromatic one. As a result, it is useful to expand the propagation constant β_m of the m-th order mode around a central frequency ω_0:

$$\beta_m(\omega) = \sum_k \frac{1}{k!} \beta_m^{(k)} (\omega - \omega_0)^k \tag{1.5}$$

where $\beta_m^{(j)} = \frac{d^j \beta_m}{d\omega^j}$ are called dispersion coefficients. These coefficients are important in the process of identifying the dispersion properties of the waveguide. For instance the first coefficient ($j = 1$) gives the inverse of the mode group velocity v_g. The second term of the expansion $\beta_m^{(2)}$ is called *group velocity dispersion* (GVD), while $\beta_m^{(3)}$ is the third-order dispersion (TOD), and so on and so forth. As anticipated, for small structures, the values assumed by the coefficients $\beta_m^{(j)}$ are dominated by the waveguide geometry, which is of essential importance in order to tailor the propagation constant using the waveguide dimensions. From the observation that the coefficients have a dependence on

the order mode, it is now clear that different modes propagate with different dispersion properties in the same waveguide, thus making the multimode propagation a very complex and exploitable tool for the nonlinear processes discussed in the next section.

It is now considered the excitation of the guided modes in a channel waveguide. The modes of such waveguide are solutions of the wave equation Eq. 1.1, and form a complete set. This means that any electromagnetic field incident at the facet of the waveguide can be expressed as a linear combination of the modes supported by the waveguide. The expansion coefficient of each mode is proportional to the power coupled on that specific mode. Using the reference frame in Fig. (1.2), it is considered a beam of laser light, arriving from $z < 0$ and impinging on the facet at $z = 0$.

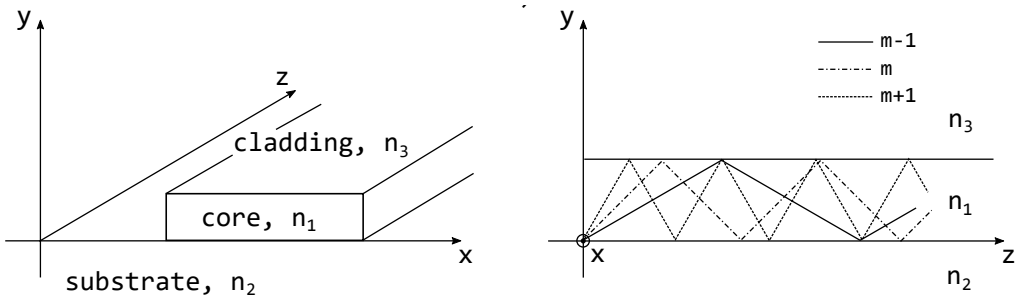

Figure 1.2: On the left hand side a schematic of the waveguide with relative reference frame. On the right hand side a representation of the propagation of different modes in the same dielectric waveguide. The smaller the angle of reflection, the smaller the order mode. Reprinted from [5].

Called $\boldsymbol{\mathcal{E}}_l$ the radiation field of the laser, than

$$\boldsymbol{\mathcal{E}}_l(x,y) = \boldsymbol{\mathcal{E}}_x(x,y) + \boldsymbol{\mathcal{E}}_y(x,y), \tag{1.6}$$

where $\boldsymbol{\mathcal{E}}_x$ and $\boldsymbol{\mathcal{E}}_y$ are the transverse electric and magnetic radiation fields, respectively.
Whereas for $z < 0$ there is only laser radiation (neglecting reflection at the facet), for $z \geq 0$ $\mathcal{E}_l$ consist of the sum of the guided modes plus a contribution from the fields radiated in the cladding, namely $\mathcal{E}_x^{rad}$ and $\mathcal{E}_y^{rad}$.
At the facet the field amplitudes for TE and TM polarization can than be written as

$$\mathcal{E}_{x,y}(x,y) = \sum_m A_m^{x,y} \psi_m^{x,y}(x,y) + \mathcal{E}_{x,y}^{rad} \tag{1.7}$$

where $\psi_m^{x,y}$ is the field profile of the m-th mode with the respective polarization (x for TE or y for TM). The coefficients A_m^x and A_m^y are the *overlap integral* that quantify the field matching between the incident radiation and

the $\psi_m^{x,y}$ mode:

$$\left|A_m^{x,y}\right|^2 = \frac{\left|\iint \mathrm{d}x\,\mathrm{d}y\ [\mathscr{E}_{x,y}\psi_m^{*\,x,y}]\right|^2}{\left[\iint \mathrm{d}x\,\mathrm{d}y\,|\psi_m^{x,y}|^2\right]^2} \tag{1.8}$$

where the integration is made over the whole space. A quite useful parameter that provides an intuitive information about the coupling efficiency for separate modes is instead the normalized *power overlap integral*

$$\Gamma_m^{x,y} = \frac{\left|\iint \mathrm{d}x\,\mathrm{d}y\,[\mathscr{E}_{x,y}\psi_m^{*\,x,y}]\right|^2}{\left(\iint \mathrm{d}x\,\mathrm{d}y\,|\psi_m^{x,y}|^2\right)\left(\iint \mathrm{d}x\,\mathrm{d}y\,|\mathscr{E}_{x,y}|^2\right)} \tag{1.9}$$

Since $\mathscr{E}_x^{rad}$ and $\mathscr{E}_y^{rad}$ radiate away after a short distance in the following they are neglected. Then, with a proper normalization of the fields and the waveguide modes $\psi_m^{x,y}$, it is possible to rewrite Eq. (1.7) as

$$\mathscr{E}_{x,y}(x,y) = \sum_m \sqrt{\Gamma_m^{x,y}}\,\psi_m^{x,y}(x,y)\,. \tag{1.10}$$

As per definition, with this normalization $\sum_m \Gamma_m^{x,y} = 1$, which is helpful for the implementation and simulation of the higher order mode coupling techniques.
In a more intuitive interpretation, the overlap integral quantifies how much the two field profiles involved in the calculation are similar: in fact the overlap integral has a maximum when the two profiles are identical. This implies that the more the field profile at the input of the waveguide resembles the profile of a given mode, the more the coupling of that mode is good.

The problem of reflection has not been considered so far, but the abrupt change of refractive index at the beginning and end of optical waveguides gives rise to a Fabry-Perot oscillation. Like in a cavity the light is continuously reflected back and forth at the input and output facets of the waveguide. From the transmission coefficient of the Fabry-Perot interferometer, it is possible to write the F-P response for a mode order m, propagating with a wavelength λ at the position z, as [6]

$$\mathscr{A}_m(\lambda,z) = \frac{(e^{-\alpha_m z} - \widetilde{R}_m)^2}{(1-\widetilde{R}_m)^2 + 4\widetilde{R}_m \sin^2(\Phi_m/2)} \tag{1.11}$$

where Φ_m is the phase acquired in one round trip and, given R_m the reflection coefficient at the waveguide/air interface, $\widetilde{R}_m = R_m e^{-\alpha_m z}$.
Considering also this internal reflection the resulting field profile propagating in the waveguide, for TE or TM polarization, can be written as

$$\boldsymbol{\mathscr{E}}_{wg}(x,y,z;\lambda) = \sum_m \sqrt{\Gamma_m(\lambda)}\sqrt{\mathscr{A}_m(\lambda,z)}\,\boldsymbol{\mathscr{E}}_m(x,y)\,, \tag{1.12}$$

where, as before, m runs over all the modes supported by the waveguide.

The control of the light propagating inside an optical waveguide is required for all the applications involving integrated photonic circuits. This can be achieved directly on-chip using a device called directional coupler (DC) [7]. This device consists simply of two parallel waveguides with a small gap in between: when two waveguides are placed sufficiently close, the evanescent field from one waveguide overlaps with the field of the other, yielding a power exchange between the two waveguides. This is a powerful tool in order to control the modes excitation in a multimode waveguide. For example, if a single mode waveguide is placed close to a waveguide with different geometry, it is possible to excite selectively one of the supported higher order modes.

1.2 Four wave mixing in optical waveguides

1.2.1 Nonlinear optical processes

Nonlinear photonics is the branch of optics that describes the behaviour of light in nonlinear media, that is, media in which the polarization density $\mathbf{P}$ responds non-linearly to the electric field $\mathbf{E} = \sum_i E_i \hat{\mathbf{a}}_i$ of the light. The nonlinearity is typically observed at very high light intensities such as those provided by lasers. At low optical powers the relation between these two quantities is

$$\mathbf{P} = \varepsilon_0 \chi^{(1)} \mathbf{E} = \varepsilon_0 \sum_{ij} \chi^{(1)}_{ij} E_i \hat{\mathbf{a}}_j \tag{1.13}$$

where ε_0 is the vacuum permittivity and $\chi^{(1)}$ is the first order susceptibility, a second rank tensor. When the input optical power increases this linear relation does not hold anymore. Moreover, in a semiconducting material free carriers and nonlinear optical effects can be important, inducing the introduction of an additional term in the polarization vector, which must be rewritten as [8]

$$\mathbf{P} = \mathbf{P}_L + \delta\mathbf{P} + \mathbf{P}_{NL}, \tag{1.14}$$

where $\mathbf{P}_L$ is the same as in Eq. (1.13), i.e. the linear polarization, $\delta\mathbf{P}$ is due to linear first-order processes associated with free carriers, while $\mathbf{P}_{NL}$ is due to nonlinear optical effects. The latter can be expanded as a series for sufficiently weak optical fields

$$\mathbf{P}_{NL} = \mathbf{P}^{(2)} + \mathbf{P}^{(3)} + \cdots = \varepsilon_0 \left[\chi^{(2)} : \mathbf{EE} + \chi^{(3)} \vdots \mathbf{EEE} + \cdots \right], \tag{1.15}$$

with $\mathbf{P}^{(2)}$, $\mathbf{P}^{(3)}$ and $\chi^{(2)}$, $\chi^{(3)}$ second and third order polarization vector and susceptibilities, respectively. The absolute value of nonlinear susceptibilities decreases with the order of the process, implying the necessity of a stronger field to achieve third order processes, with respect to second order ones. In general $\chi^{(j)}$ would be a tensor of rank $(j+1)$, but for isotropic media (such as silicon dioxide) they can be regarded as scalar quantities. Silicon, however,

is not amorphous and has a centrosymmetric crystalline structure. This type of symmetry prevents the existence of even order nonlinearities, still allowing odd order ones.

Second order nonlinear processes

The second order is the lowest order for a nonlinear process in a non centrosymmetric medium and, although not present in integrated silicon photonics, second order processes have a whole lot of experimental applications. Let us consider two optical fields (having frequencies ω_1 and ω_2) with equal amplitudes interacting in a medium, let $\mathbf{E}_1$ and $\mathbf{E}_2$ be the respective electric fields, the second order polarization vector can then be expressed as [8]

$$\begin{aligned}\mathbf{P}^{(2)}(\mathbf{r},t) =& \varepsilon_0\chi^{(2)} : \left[\mathbf{E}_1(\mathbf{r},\omega_1)\mathbf{E}_1(\mathbf{r},\omega_1)e^{-i2\omega_1 t} + \mathbf{E}_2(\mathbf{r},\omega_2)\mathbf{E}_2(\mathbf{r},\omega_2)e^{-i2\omega_2 t}\right] \\ &+\varepsilon_0\chi^{(2)} : \left[2\mathbf{E}_1(\mathbf{r},\omega_1)\mathbf{E}_2(\mathbf{r},\omega_2)e^{-i(\omega_1+\omega_2)t}\right] \\ &+\varepsilon_0\chi^{(2)} : \left[2\mathbf{E}_1(\mathbf{r},\omega_1)\mathbf{E}_2^*(\mathbf{r},\omega_2)e^{-i(\omega_1-\omega_2)t}\right] \\ &+\varepsilon_0\chi^{(2)} : \left[\mathbf{E}_1(\mathbf{r},\omega_1)\mathbf{E}_1^*(\mathbf{r},\omega_1) + \mathbf{E}_2(\mathbf{r},\omega_2)\mathbf{E}_2^*(\mathbf{r},\omega_2)\right] + c.c.\end{aligned}$$

The terms of the first line gives origin to SHG (second harmonic generation), where two photons with the same frequency are interacting within a nonlinear medium to generate a new photon with twice the energy of the incident photons. The term of the second line, instead, refers to SFG (sum frequency generation). In this case two photons with different frequencies ω_1

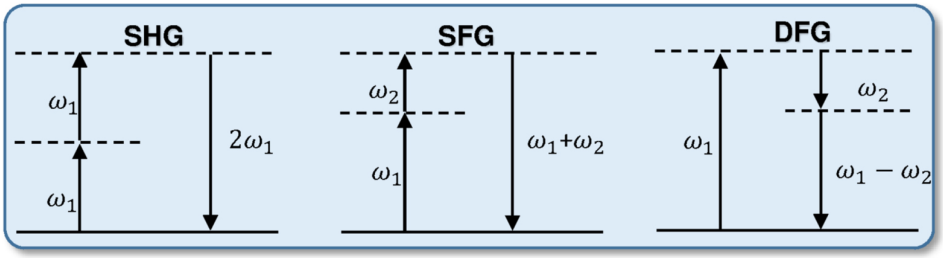

Figure 1.3: Virtual state diagram of the second-order processes whose description is given by the first three terms of $\mathbf{P}^{(2)}$. From the left: SHG, SFG, and DFG. Reprinted from [8].

and ω_2 annihilate to produce the third photon with frequency $\omega_1 + \omega_2$. In analogy with SFG the third line represents DFG (difference frequency generation), where the generated photon has a frequency $\omega_1 - \omega_2$. Lastly the fourth term represents optical rectification (OR), i.e. a process that gives rise to the generation of a DC component of the polarization.

Third order nonlinear processes

Third order nonlinear processes consists of the superposition of three waves ($\mathbf{E}_1$, $\mathbf{E}_2$, $\mathbf{E}_3$), that generates a fourth one. Following the approach used for

the second-order case, the polarization vector $\mathbf{P}^{(3)}(\mathbf{r},t)$ can be written as the summation of various terms, each one corresponding to different processes [9]:

$$\begin{aligned}\mathbf{P}^{(3)}(\mathbf{r},t) = \varepsilon_0\chi^{(3)} \vdots \Big[& \mathbf{E}_1(\mathbf{r},\omega_1)\mathbf{E}_1(\mathbf{r},\omega_1)\mathbf{E}_1(\mathbf{r},\omega_1)e^{-i3\omega_1 t} \\ & + 3\mathbf{E}_1(\mathbf{r},\omega_1)\mathbf{E}_1(\mathbf{r},\omega_1)\mathbf{E}_2(\mathbf{r},\omega_2)e^{-i(2\omega_1+\omega_2)t} \\ & + 3\mathbf{E}_1(\mathbf{r},\omega_1)\mathbf{E}_1(\mathbf{r},\omega_1)\mathbf{E}_2^*(\mathbf{r},\omega_2)e^{-i(2\omega_1-\omega_2)t} \\ & + 6\mathbf{E}_1(\mathbf{r},\omega_1)\mathbf{E}_2(\mathbf{r},\omega_2)\mathbf{E}_3(\mathbf{r},\omega_3)e^{-i(\omega_1+\omega_2+\omega_3)t} \\ & + 6\mathbf{E}_1(\mathbf{r},\omega_1)\mathbf{E}_2(\mathbf{r},\omega_2)\mathbf{E}_3^*(\mathbf{r},\omega_3)e^{-i(\omega_1+\omega_2-\omega_3)t} \\ & + 3\mathbf{E}_1(\mathbf{r},\omega_1)\mathbf{E}_1^*(\mathbf{r},\omega_1)\mathbf{E}_1(\mathbf{r},\omega_1)e^{-i\omega_1 t} \\ & + 6\mathbf{E}_1(\mathbf{r},\omega_1)\mathbf{E}_2(\mathbf{r},\omega_2)\mathbf{E}_2^*(\mathbf{r},\omega_2)e^{-i\omega_1 t}\Big] + c.c.\end{aligned} \tag{1.16}$$

For sake of clarity, in this formula the permutation of the photon indices (i.e. of the waves) has been omitted.
In analogy with SHG, the first term is the third harmonic generation (THG), that refers to the generation of one photon at a $3\omega_1$ frequency, after the annihilation of three photons at ω_1. The second to fifth elements of the summation are responsible for four-wave mixing (FWM), where four photons combine to give rise to the generation of new harmonics. Various combinations of this type are possible, but the most common is the one shown in Fig. 1.4. Here the annihilation of two incident photons, the *pump* photons, generate two other frequencies, the *idler* and the *signal* photons. The sixth term of the summation

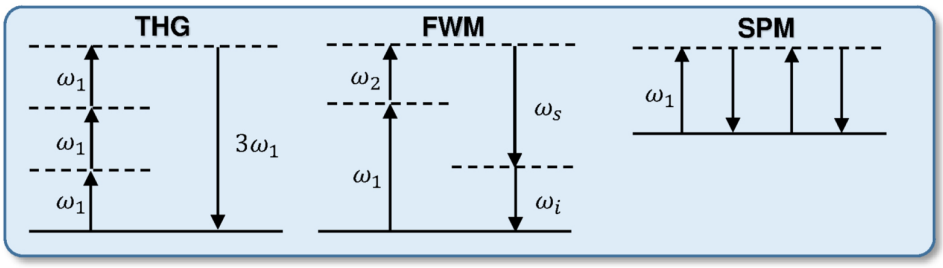

Figure 1.4: Virtual state diagram of some third-order nonlinear processes. From the left: THG, FWM, and SPM. Reprinted from [8].

in the $\mathbf{P}^{(3)}(\mathbf{r},t)$ expression, is the one responsible for both self-phase modulation (SPM) and TPA (two-photon-absorption). In particular SPM is related to the real part of the third-order susceptibility, while TPA is related to the imaginary part of $\chi^{(3)}$. The last term of Eq. (1.16) is responsible for the cross-phase modulation (XPM).
It should be noticed, en passant, that so far only electronic contributions to third-order nonlinear susceptibility have been considered. However, in general one should also consider the role of phonons in order to get a correct $\chi^{(3)}$. This contribution can be represented by the Raman susceptibility $\chi_R^{(3)}$, which involves Raman optical phonons [8]. In this framework, additional terms are

present in the polarization vectors, thus increasing the zoo of third-order nonlinear processes.

The large family of optical nonlinear processes can be grouped into two main categories, parametric and nonparametric processes. A parametric process is a process in which the initial and final quantum mechanical states of the system are identical [10]. For this reason the initial energy is conserved in the form of photons and, in addition, also momentum and angular momentum are not transferred from or to the material medium.
In contrast, a nonparametric process is a process in which the energy can be exchanged with the material also through other forms, like heat or sound. In general parametric processes can always be associated with a real susceptibility, on the contrary, nonparametric processes are described by a complex susceptibility. All the second and third order processes described above are parametric, except the ones including phonons and TPA, in which photon energy goes into the excitation of free carriers.

As for third order nonlinearities in silicon, four-wave-mixing is the most studied process since it can be used for a wide range of applications, such as entangled photon generation, wavelength conversion, optical phase conjugation and optical isolation [11, 12, 13]. In the following the most common FWM interaction will be taken into consideration, i.e. the previously shown process in which the two input photons are annihilated to generate an idler-signal pair (Fig. 1.5).

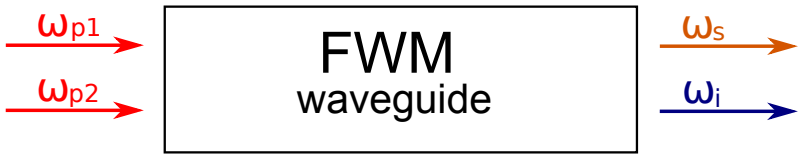

Figure 1.5: Schematization of a four wave mixing process: the two different pump photons are injected from the facet of the waveguide and are subsequently converted into the signal and idler frequencies.

When the two pump frequencies are equal, the FWM process is called degenerate FWM (DFWM). There is an additional distinction based on the presence or not of a stimulating signal along with the pump. When at the input of the system only the pump waves are provided, the FWM can spontaneously generate both the idler and the signal waves, and the process is called spontaneous FWM (SFWM). When, instead, together with the pump, also a stimulating signal is provided at the frequency of the signal or of the idler, the process is called stimulated FWM (sFWM). While the latter can be described with a classical electromagnetic theory, the former requires a quantum mechanical description, being stimulated by the vacuum quantum fluctuations. An important feature of spontaneous FWM is that the generated idler and signal photons are always emitted simultaneously in pairs and their degree of correlation depends on the bandwidths of both the pump (ω_{p1}, ω_{p2}) and the generated photons themselves (ω_s, ω_i). This characteristic lays at the basis of

the use of FWM for the generation of entangled and single photon states. For future reference, it is called 'idler' the photon at higher frequency and 'signal' the photon at lower frequency.
Of course the generated bandwidth must comply with energy conservation, that one can write as

$$\hbar\omega_{p1} + \hbar\omega_{p1} = \hbar\omega_s + \hbar\omega_i. \tag{1.17}$$

However that is not the only constraint, in fact the process is not independent of the phase of the waves involved: the generated waves in the medium add up constructively if they are properly matched in phase. The *phase matching condition* basically correspond to the momentum conservation as follows

$$k_{p1} + k_{p2} = k_s + k_i. \tag{1.18}$$

It is noteworthy that these nonlinear processes can occur even if Eq. (1.18) is not satisfied. In fact the total momentum conservation (and maximum FWM efficiency) is achieved through particular techniques that phase match the waves. Otherwise, the bigger the phase mismatch

$$\Delta k = k_{p1} + k_{p2} - k_s - k_i, \tag{1.19}$$

the lower the generation efficiency.

1.2.2 Four wave mixing phase matching

One can develop the classical theory of FWM in waveguides, starting from the wave equation Eq. (1.1) and taking into account also the nonlinear polarization. As it turns out, $\mathbf{P}_{NL}$ has the role of a source that radiates in a linear medium of refractive index n:

$$\nabla^2\mathbf{E}(\mathbf{r},\omega) + \frac{\omega^2}{c^2}n^2\mathbf{E}(\mathbf{r},\omega) = -\frac{\omega^2}{\varepsilon_0 c^2}\mathbf{P}_{NL}(\mathbf{r},\omega). \tag{1.20}$$

Developing further the theory, it can be shown that the efficiency η of standard and spontaneous FWM scales with the phase mismatch as [5]

$$\eta \propto |f_{p1p2si}|^2 L^2 \,\mathrm{sinc}^2\left(\Delta k\frac{L}{2}\right) \tag{1.21}$$

where L is the nonlinear medium length, f_{p1p2si} is the mode field overlap, with $p1$, $p2$, s, i indicating, respectively, the mode orders for the two pump photons, the signal, and the idler photons.
Since the nonlinear waves can interact constructively only for a limited length in the medium, it comes naturally, starting from the previous expression, to introduce a *coherence length* for the process as

$$L_{coh} = \frac{\pi}{\Delta k}. \tag{1.22}$$

L_{coh} indicates the length over which the nonlinear interaction is constructive. In other terms, beyond this length the pump and the generated wave get out of phase when a phase mismatch Δk is present.

For sake of completeness, it is convenient to point out that the phase mismatch used above is the sum of a linear contribution, given by Eq. (1.19), and a nonlinear one Δk_{NL}. This last nonlinear term quantifies the phase contribution to Δk due to the self-phase modulation (SPM) of the pumps and can be written as

$$\Delta k_{NL} = \gamma_{P1} P_{P1} + \gamma_{P2} P_{P2}, \tag{1.23}$$

where γ_{P1} and γ_{P2} are nonlinear coefficients for the two pumps, and P_{P1}, P_{P2} are the powers of the two pumps. The phase induced by SPM becomes important only when very high pump intensities are involved, thus with small cross-section waveguides or with high peak powers. Based on the fact that multimode waveguides are characterized by large cross-sections and low intensities, from here on this contribution will be neglected.

Before introducing intermodal four wave mixing it is worth making further phase matching considerations. The phase matching issue arises from the chromatic dispersion of the medium, by which the refractive index of the medium increases nonlinearly and monotonically with the frequency, namely $k(\omega) = n(\omega)\omega/c$.
It has been already discussed the possibility to act on the geometry of the waveguide in order to tailor the dispersion experienced by the guided light. Using the propagation constants, the phase mismatch ($k \equiv \beta$) for a single mode DFWM process can be written as

$$\Delta\beta = 2\beta(\omega_p) - \beta(\omega_s) - \beta(\omega_i). \tag{1.24}$$

One can then Taylor expand the propagating constants around the frequency ω_p, as per Eq. (1.5). Since all odd terms of the expansions cancel each other out, it is straightforward to demonstrate that the phase mismatch results

$$\Delta\beta = -\beta_2(\omega_p)\Delta\omega^2 - \frac{1}{12}\beta_4(\omega_p)\Delta\omega^4 - \ldots, \tag{1.25}$$

where $\Delta\omega = \omega_i - \omega_p = \omega_p - \omega_s$. As a first approximation one could think of achieving perfect phase matching with $\beta_2 = 0$. But in this case also the small negative nonlinear contribution given by SPM would not allow a total phase matching: in order to get $\Delta\beta = 0$ the β_2 term should be negative, fact often referred to as anomalous GVD [14].
Now, from Eq. (1.21) one can consider $\Delta k_{max} = \Delta\beta_{max} = 4/L$ as the maximum tolerable loss of efficiency. Taking only the first term in Eq. (1.25), this result will lead to an expression that links L and the bandwidth of the process:

$$BW \approx \sqrt{\frac{\Delta\beta_{max}}{\beta_2\omega_p}} = \sqrt{\frac{4}{L\beta_2\omega_p}}. \tag{1.26}$$

Obviously as soon as the detuning $\Delta\omega$ increases, also higher order terms in the expansion become essential to perform a correct phase matching (PM). In this context comes up naturally a distinction between the so called *continuous*

band phase matching and *discrete band phase matching*. The former arises when the phase matching band is centered at the pump wavelength. The discrete band phase matching, instead, happens when the PM bandwidth is centered at the phase matching wavelength. Typically, in this case, the detuning is so big that is necessary to consider the first two terms in Eq. (1.25) and the phase matching is achieved when $\beta_2(\omega_p)$ and $\beta_4(\omega_p)$ have opposite sign, thus using higher order term to compensate the phase mismatch carried by the GVD term. This implies that GVD compensation can be achieved only far from the pump wavelength, making this process not suitable for all those applications requiring a tunable wavelength conversion.
An important limit of single mode FWM is that the β_2 value is critically dependent on the geometry of the waveguide, which makes the engineering of the dispersion a non trivial task. As a matter of fact, as shown in Fig. 1.6 a), a small variation of the waveguide affects critically the phase matching.

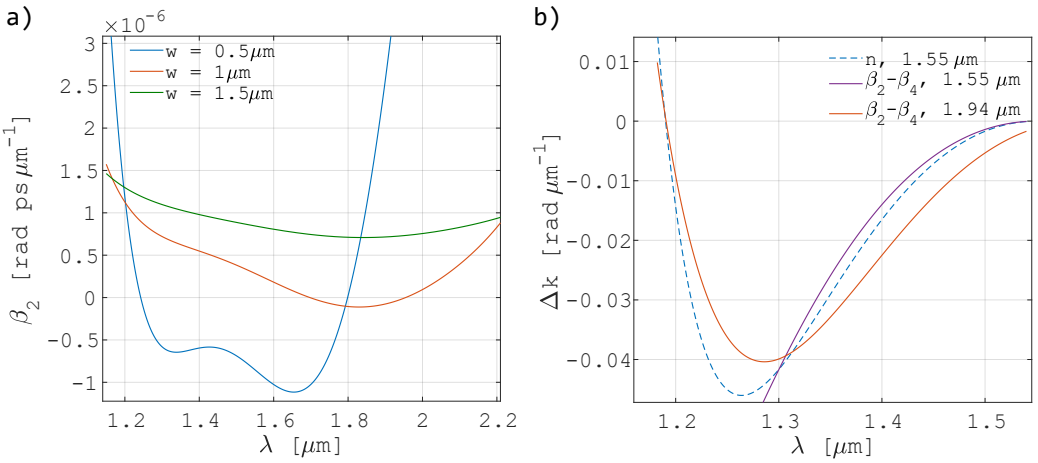

Figure 1.6: a) GVD dependence on the wavelength, for different waveguide widths. b) Δk vs idler wavelength. Simulation for a 2 μm wide and 243 nm high waveguide. It is compared the phase mismatch calculated with the dispersion compensation and from Eq. (1.24). Reprinted from [5].

Moreover, when considering a practical implementation, the GVD terms are not a reliable tool, indeed the higher order terms of the expansion in Eq. (1.25), are much more important than what expected, as can be seen in Fig. 1.6 b). Here, the dispersion compensation method fails to calculate the phase matching position using the correct 1.55 μm pump wavelength, but the PM in the expected position is recovered with a 1.94 μm wavelength.
A viable solution in order to face these drawbacks, is to take advantage of the higher order modes propagating in a multimode waveguide. Using different waveguide modes gives one more degree of freedom to engineer the phase matching. This is the case of *intermodal phase matching*, where different order waveguide modes are used.

1.2.3 Intermodal four wave mixing

Four wave mixing is the most studied and exploited nonlinear process in silicon photonics, and it is usually used in its intramodal configuration, i.e. using only one waveguide mode. Intermodal FWM (IFWM in the following), instead, is based on the excitation of different order modes, enabling functionalities that are not easily accessible to single mode FWM: thanks to this process it is possible, for instance, to generate light with highly controllable wavelengths and bandwidth, enabling spectral conversions which can link the NIR with the MIR part of the spectrum. These results are extremely attractive for integrated photonics, which is striving for devices able to perform all optical wavelengths conversion for signal processing.
In addition to the anticipated advantages of intermodal FWM, there is also the fact that anomalous GVD dispersion is not needed in order to achieve phase matching, as instead happens for intramodal FWM [14]. This results in an easier handling of the phase-matching condition: the IFWM exhibits higher flexibility, larger spectral conversion, and easier phase matching.

For the control of the phase matching condition it is essential to engineer the index dispersion through the geometry of the waveguide. Moreover, it is possible to select the effective index value of the propagating wave by excitation of a specific optical mode, as shown in Fig. 1.7.

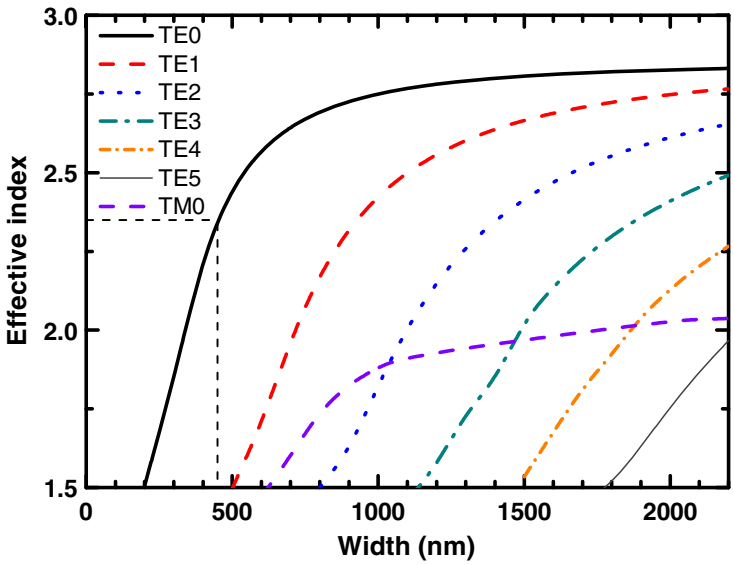

Figure 1.7: Effective indices as a function of the width of the TE modes and the fundamental TM mode supported by a 220 nm high SOI strip waveguide with silica cladding. Reprinted from [15].

As a consequence, in contrast with intramodal FWM, the effective pump indexes n_{eff} for a DFWM process are not the same in general. Since the wavevector depends on the index as $k = \frac{\omega}{c} n_{\text{eff}}$, this introduce a major difference in the

conservation constraints

$$\begin{cases} \omega_p + \omega_p = \omega_s + \omega_i \\ k_{p1} + k_{p1} = k_s + k_i \end{cases} \tag{1.27}$$

In fact, the linear phase mismatch in a multimode waveguide, not considering nonlinearities due to the SPM of the pumps, becomes

$$\Delta k_L = \frac{\omega_p}{c} n_{\text{eff}}^{p_1}(\omega_p) + \frac{\omega_p}{c} n_{\text{eff}}^{p_2}(\omega_p) - \frac{\omega_s}{c} n_{\text{eff}}^{s}(\omega_s) - \frac{\omega_i}{c} n_{\text{eff}}^{i}(\omega_i), \tag{1.28}$$

where $p1$, $p2$, i, s refer to the order modes of the two pumps, the signal and the idler, respectively.
As already pointed out, the most common scenario for the modes configuration is $p1 = p2 = s = i$, that correspond to standard intramodal FWM. For IFWM, instead, the more feasible are $p1 = p2 \neq s = i$ and $p1 = s \neq p2 = i$. The first one refers to the case of the two pumps on one mode and the signal and idler on another one, while in the latter one pump has the same mode of the signal, and the other pump propagates on the same mode of the idler.

In order to deal with different order modes, for the group dispersion terms it is used the notation $\beta_{n,m}$, where the index n identifies the n-th term of the Taylor expansion, while m is the mode order.
Let us briefly consider the mode combination $p1 = p2 \neq s = i$ for DFWM. Expanding the dispersion constants around ω_p and truncating it at the fourth order coefficient, the phase mismatch can be written as

$$\Delta\beta = 2(\beta_{0,p1} - \beta_{0,s}) - \beta_{2,s}\Delta\omega^2 - \frac{1}{12}\beta_{4,s}\Delta\omega^4 \tag{1.29}$$

This modes combination has many similarities with the intramodal case, the main difference being the presence of the first term. As a consequence of this term the phase matching cannot be achieved at small values of detuning ($\Delta\omega \sim 0$), as instead happens in the intramodal case.

For $p1 = s \neq p2 = i$, we consider again the case of degenerate FWM ($\omega_{p1} = \omega_{p2} = \omega_p$) and an expansion around ω_p. The phase mismatch up to the fourth order dispersion term is

$$\begin{aligned} \Delta\beta = &-(\beta_{1,i} - \beta_{1,s})\Delta\omega - \frac{1}{2}(\beta_{2,i} + \beta_{2,s})\Delta\omega^2 \\ &-\frac{1}{6}(\beta_{3,i} - \beta_{3,s})\Delta\omega^3 - \frac{1}{22}(\beta_{4,i} + \beta_{4,s})\Delta\omega^4. \end{aligned} \tag{1.30}$$

As a first approximation let us consider just the first line in Eq. (1.30). In analogy with the intramodal case, the first term in the equation, which is just the group velocity mismatch of the output signals, could be compensated by the second order term of idler and signal. In a situation where $\beta_{1,s} > \beta_{1,i}$ the second order term does not need to be negative, which means that anomalous

GVD is not necessary. On the other hand if $\beta_{1,s} < \beta_{1,i}$, than β_2 needs to be negative for at least one of the two output modes.
Again as soon as the detuning $\Delta\omega$ increases, the third and fourth order terms in the expansion become essential to perform a correct PM.
Fig. 1.8 compares the frequency dependence of the idler generation efficiency, from Eq. (1.21), for the intramodal and intermodal DFWM. When no compen-

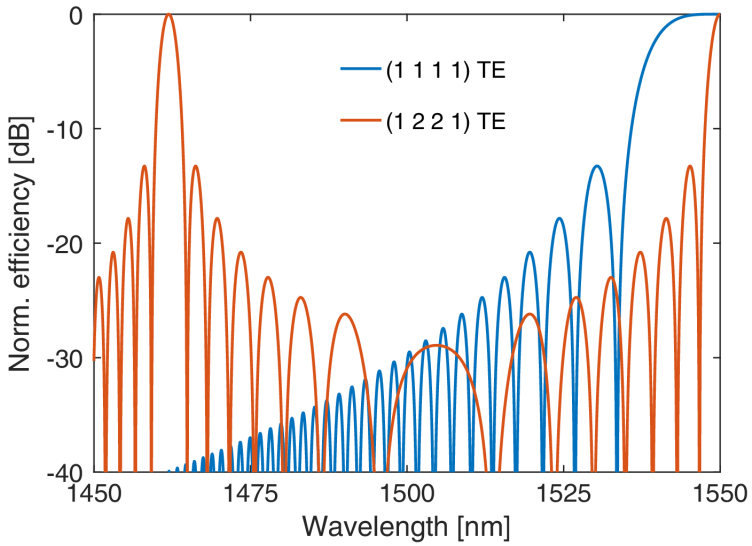

Figure 1.8: Normalized idler generation efficiency vs wavelength. Pump photons at 1.55 μm, comparison of the 1111TE intramodal combination and the 1221TE intermodal one. Simulation for a 3.5 μm wide and 243 nm high silicon waveguide. Reprinted from [7].

sation is present for the intramodal case, the IFWM exhibits a discrete phase matching that can be tuned far from the pump. Intramodal FWM, instead, displays phase matching only close to the pump wavelength.

The mode field overlap, already introduced in Eq. (1.21), reveals itself as a powerful tool to quantify the coupling between the field involved in the FWM process. Furthermore, it is a useful parameter to estimate confinement, resulting in a higher value when the modes are more confined in the waveguide core. For the aforementioned intermodal configuration $(p1, p2, s, i)$, it is given by [7]

$$f_{p1p2si} = \frac{\int_{A_0} E_{p1}(r,\omega_{p1}) E_{p2}(r,\omega_{p2}) E_s^*(r,\omega_s) E_i^*(r,\omega_i) A}{\prod_{k=p1,p2,s,i} \left[\int_{A_\infty} n_{wg}^2(r,\omega_k) |E_k(r,\omega_k)|^2 A \right]^{\frac{1}{2}}}, \qquad k = p1,\ p2,\ s,\ i,$$

where r is the spatial coordinate in the cross-section plane, A_0 is the waveguide cross section itself and A_∞ is the whole transverse plane. The waveguide refractive index is n_{wg}, while E_k is the mode field of each wave. The form of f_{p1p2si} suggests that not all the modal combinations are possible, since an odd integrand at the numerator would result in a zero efficiency process.

From the works of Signorini et al. [5, 7], it is clear that involving higher order modes in the FWM process affects negatively the efficiency of the process, which is reduced by the smaller mode field overlap, with respect to the intramodal case. It is shown that, in terms of efficiency, the intermodal combinations perform better when the combination is symmetric. When, instead, one mode is different from the others, the relative efficiency decreases dramatically. Moreover, comparing TM polarization combinations with respect to the TE case, it can be seen that the latter are more efficient due to their larger mode area.
Notwithstanding its lower efficiency with respect to intramodal FWM, the intermodal approach enables larger spectral translations and opens new functionalities for technologies involving higher order modes. In the aforementioned works, in fact, it is also observed that, as the pump wavelength is increased, the spectral position of the phase matching condition moves towards longer wavelengths.

Chapter 2

Heralded single photon sources

At the beginning of this chapter are briefly discussed the basics of single photon sources, with a particular attention on heralded sources. Next, the major experimental parameters for the characterization of heralded single photon sources are summarised. In the end there will be a presentation of the chip that implements the heralded single photon source whose results are shown in the next chapter, as well as the experimental set-up used for its characterization.

2.1 Basics of single photon sources

Quantum mechanics is present at the roots of many scientific and technological advancements that have had an indelible effect on our society, including high-performance computation, secure communication, high-sensitivity metrology and sensing. The major driver of the current research into single-photon sources is probably the exponential growth of the field of quantum-information over the last decades. Research has shown that using quantum objects in order to encode, manipulate, and measure information allows some computational tasks to be performed more efficiently than thought possible using classical objects [16, 17, 18]. Photonic qubits, in analogy with the classical bits, are the basic unit where information can be encoded. Information can be written in the quantum state exploiting the photon degrees of freedom (polarization, momentum, energy, etc.) [19]. Moreover, since photons interact weakly with their environment over long distances, they are affected by limited decoherence, enabling room temperature operation. A further non-negligible advantage in the quantum information framework, is that photons can be transmitted within the already world-wide deployed optical fiber network.
Quantum computing architectures and hardware platforms are highly demanding in terms of components, requiring thousands of components to work properly. Therefore developing such technologies on integrated photonic chips is key in order to move them outside the laboratory. Silicon photonics is the ideal solution thanks to its mature fabrication technology, which allows high density device integration. The main components of quantum photonic systems, such as interferometers, beam splitters, phase shifters, etc. are all now realisable in

an integrated form [20]. As for sources of non-classical light, single photons can be generated in different ways, e.g. atom-like emitters, as trapped ions or quantum dots, or heralded sources based on correlated photon pairs [21].

The ideal single photon source would be one for which a single photon is emitted at any arbitrary time defined by the user (i.e. the source is deterministic, or "on-demand"), with a probability of emission of 100%. Moreover, the probability of multiple-photon emission should be 0%: this concept is often referred to as the "photon gun" [22], where by pressing a button a single photon is emitted instantaneously with unit probability. Carrying on the analogy, the bullets should be identical from shot to shot: in an ideal single photon source, the emitted photons are indistinguishable [23]. In real-world sources, deviations from these ideal characteristics are always present. Deterministic sources, that are often based on atom-like emitters, are in general more efficient than probabilistic ones, but despite the high performance of such sources, their integration in a photonic integrated circuit is still an open issue, due to high coupling losses, not reproducible fabrication and the need of cryogenic working temperatures [24].
A valid alternative which solves these issues is the probabilistic heralded single photon source. This source rely on photons created in pairs via parametric downconversion (PDC) in bulk crystals and waveguides, or four-wave mixing (FWM) in optical waveguides. These sources are said to be probabilistic since the creation of photon pairs is not guaranteed, but happens with a certain probability. However, because the photons are created in pairs, the detection of one photon, the *herald*, can be used to confirm the creation of the other photon, the *heralded* one, that can be used as a single photon in the quantum device.

2.1.1 Elements of photon statistics

Let us consider an ensemble of photons, each one characterized by a photon state (with a defined polarization, frequency and spatial mode): if all photons occupy the same state, than this ensemble is represented by a pure state. A general pulse of light in quantum optics can be a linear combination of several pure states: in the following such states are identified by $|n\rangle$. Here, n denotes the number of photons in this particular state (called Fock state), that is an eigenstate of the single-mode number operator $\hat{n}$, whose eigenvalue is n. For future reference it is useful to introduce the photon number creation ($\hat{a}^\dagger$) and destruction ($\hat{a}$) operators as

$$\begin{aligned} \hat{a}^\dagger |n\rangle &= \sqrt{n+1}\,|n+1\rangle\,, \\ \hat{a}\,|n\rangle &= \sqrt{n}\,|n-1\rangle\,, \end{aligned} \tag{2.1}$$

from which it is straightforward to see that $\hat{n} = \hat{a}^\dagger \hat{a}$.
A parametric photon pair source generates quantum states that, if the two

photon beams emitted are on a single-mode, can be written as

$$|\psi\rangle_{pair} = \sum_{n=0}^{\infty} \xi_n |n\rangle_a |n\rangle_b , \tag{2.2}$$

where a and b identify the two beams emitted and $|\xi_n|^2$ is the probability $P(n)$ to find n photons both in a and b. What is expected from a spontaneous parametric process is that the number of photons in the two beams is the same. As a consequence an ideal single-mode photon pair source should produce a quantum state with $P(1) = 1$, i.e. $|\psi\rangle_{pair} = |1\rangle_a |1\rangle_b$. In real-world sources, however, the probability of non emitting at all ($P(0) \neq 0$) or to emit multi-photon pairs ($P(n > 1) \neq 0$) is far from being negligible.
To tackle this issue the heralding process is introduced: the intrinsic temporal correlations of paired photons are used to kill $P(0)$ and enhance the $P(1)$. The quantum state of a single photon source can be described analogously to the photon pair source using again $P(n)$ as the probability to detect n photons in the output beam. Since through the heralding process the probability of detecting zero photons is so low, the probability of single detection $P(1)$ increases dramatically (Fig. 2.2) with respect to the mere observation of a single beam of the photon pair source (Fig. 2.1).

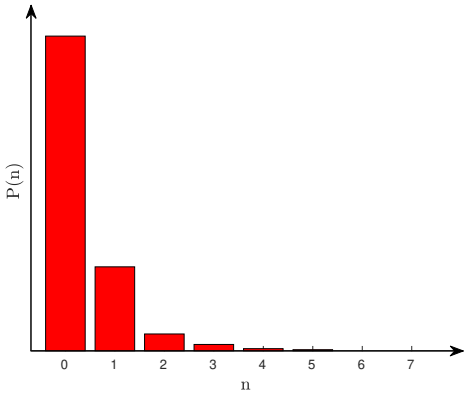

Figure 2.1: Normalized photon number distribution for a single beam of the photon pair source.

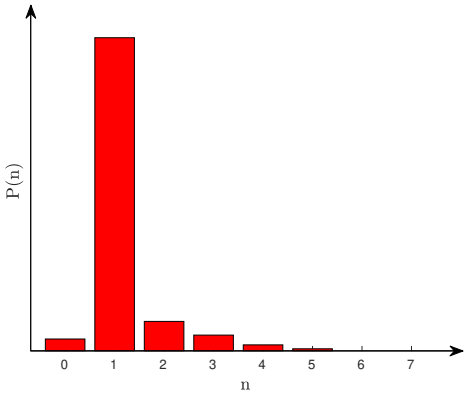

Figure 2.2: Normalized photon number distribution for the heralded beam of the photon pair source.

A useful tool in order to quantify the multi-photon emission probability is a time and position correlation function that is called *second order coherence*, or $g^{(2)}$. The $g^{(2)}$ measures the statistics of the source, taking into account the spatial and temporal correlations between the emitted photons. Since the correlation function is an ensemble average, when a stationary source is considered (it is the case of a pump given by a continuous wave laser), the only information that matters about the time of the two modes is their difference Δt. Moreover, for photon sources only one mode is measured and at the same position. In this context the second order coherence can be written as [25]

$$g^{(2)}(\Delta t) = \frac{\langle \hat{a}^\dagger(t)\hat{a}^\dagger(t+\Delta t)\hat{a}(t+\Delta t)\hat{a}(t)\rangle}{\langle \hat{a}^\dagger(t)\hat{a}(t)\rangle^2} \tag{2.3}$$

where the angled brackets indicate an ensemble average. When pulsed sources are used, the time can be discretized with the pulse number, and the $g^{(2)}$ is written as

$$g^{(2)}[m] = \frac{\langle \hat{a}^\dagger[l]\hat{a}^\dagger[l+m]\hat{a}[l+m]\hat{a}[l]\rangle}{\langle \hat{a}^\dagger[l]\hat{a}[l]\rangle^2} \tag{2.4}$$

where $l, m \in \mathbb{N}$ indicate the pulse number and the ensemble average is made over the l index. In both continuous wave (CW) and pulsed sources cases, the non-zero delay $g^{(2)}$ can be rewritten as

$$g^{(2)}(0) = \frac{\langle \hat{n}(\hat{n}-1)\rangle}{\langle \hat{n}\rangle^2} = \frac{\langle \hat{n}^2\rangle - \langle \hat{n}\rangle}{\langle \hat{n}\rangle^2}. \tag{2.5}$$

The theoretical conclusions derived from the $g^{(2)}$ are independent on the pulsed or CW formalism. From now on it is used the CW notation without loss of generality.
From Eq. (2.5), the $g^{(2)}(0)$ is directly related to the photon number emission probabilities. An ideal single photon source is expected to have $\langle \hat{n}\rangle = 1$, that implies a zero second order coherence.

Three regimes of statistical distributions can be associated to a light source: Poissonian, super-Poissonian and sub-Poissonian. The distinction is defined by the relationship between the variance and the average photon number of the source. Once that the photon number variance $\Delta n^2 = \langle \hat{n}^2\rangle - \langle \hat{n}\rangle^2$ is defined, a Poissonian photon statistics corresponds to the case $\Delta n^2 = \langle \hat{n}\rangle$. This is the case of coherent light. One can rearrange Eq. (2.5) and write it in the more suitable form

$$g^{(2)}(0) = 1 + \frac{\Delta n^2 - \langle \hat{n}\rangle}{\langle \hat{n}\rangle^2}, \tag{2.6}$$

from which it is clear that a Poissonian statistics implies $g^{(2)}(0) = 1$, i.e. no correlation whatsoever between the photons.
When the variance of the photon number is larger than the average photon number, the photon statistics is said to be super-Poissonian ($g^{(2)}(0) > 1$). Oppositely, if $g^{(2)}(0) < 1$ the variance is smaller than the average of the photon number and a sub-Poissonian statistics is characterizing the light.
For a super-Poissonian light, which is the case for thermal sources, the large variance implies that photons arrive more probably closely spaced in time rather than far apart: it is said that they reach the detectors in bunches. The sub-Poissonian light, on the contrary, presents an antibunching behaviour, i.e. photons are regularly emitted in time, but never together. As a consequence when bunching occurs the second order coherence is peaked at $\Delta t = 0$, while for sub-Poissonian light a dip is present for the zero-delay $g^{(2)}$ (Fig. 2.3).

An ideal single photon source implies $g^{(2)}(0) = 0$, thus an anti-bunching behaviour. Nevertheless a slight evidence of anti-bunching is not enough to

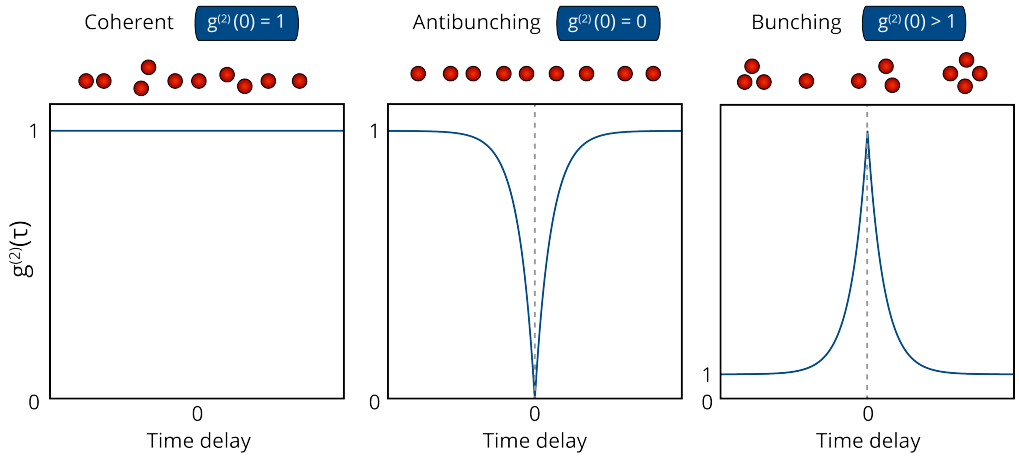

Figure 2.3: Second-order coherence $g^{(2)}(\tau = \Delta t)$ for various light sources, from the left: Poissonian, super-Poissonian and sub-Poissonian. The red balls represent a schematic photon distribution in time for that particular $g^{(2)}$ curve.

claim a single photon emission. In fact, rewriting Eq. (2.5) as a function of the number of photons in a pulse (n) we find

$$g^{(2)}(0) = \frac{\langle n|\,\hat{n}(\hat{n}-1)\,|n\rangle}{\langle n|\,\hat{n}\,|n\rangle^2} = 1 - \frac{1}{n}, \tag{2.7}$$

From Eq. (2.7), the zero-delay second order coherence for a Fock state with $n = 2$ photons results 0.5, thus suggesting the presence of the anti-bunching dip even if there is multi-photon generation. Therefore, to demonstrate the single photon emission character of a source, a $g^{(2)}(0) < 0.5$ should be measured.

Experimentally, the $g^{(2)}$ can be measured by means of a Hanbury-Brown and Twiss (HBT) interferometer with click/no-click detectors. In the HBT in-

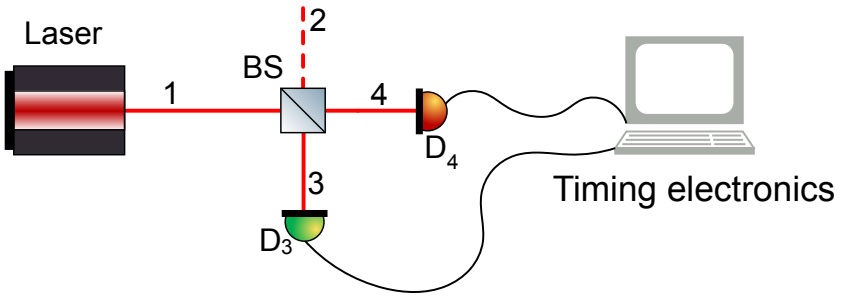

Figure 2.4: Schematics of a HBT interferometer with a generic laser beam as input signal at port 1; in the input port 2 the vacuum field is present. The output detection signals coming from the two detectors are analyzed by timing electronics, such as a time tagger.

terferometer, whose setup is shown in Fig. 2.4, the single photon beam enters from the input port 1 of the beam splitter and is then measured by one of

the two detectors (D3 and D4) placed in the reflected and transmitted ports (ports 3 and 4 respectively). Both the electric signals from detectors D3 and D4, triggered by the detection of the photon beams, are then processed by the counting electronics which stores coincidence events and their timing. The intuitive concept behind the HBT experiment is that if only one photon at a time enters the beam splitter, there is no chance that both D3 and D4 can detect it, yielding zero coincidences at zero delay.
HBT interferometry is used to give a $g^{(2)}(\Delta t)$ estimate by applying a Δt temporal shift to one of the two detectors. Moreover, the second order coherence is modified neither by asymmetries in the transmission and reflection coefficients of the beam splitter, nor by the efficiencies of the click detectors.

2.2 Heralded single photon sources parameters

In this section a brief introduction to the main experimental parameters and metrics for the characterization of heralded single photon sources is provided.

2.2.1 Purity

A major requirement for a single photon source is the purity of the generated state, that is basically the measurement of the single mode emission character of the generated single photon. In fact, several quantum information applications are based on the interference of two or more single photons and, in this framework, pure states are required for optimal visibility quantum interference [26]. Completely unentangled photons would be the perfect information carriers for these functions, but when dealing with heralded single photon sources, an issue comes up since the photon pair is inherently generated in an entangled state. As a consequence of the detection of the heralding photon, the heralded one is projected into a mixed state. Intuitively, purity measures how much the photons are entangled, with $P = 1$ completely unentangled photons and $P = 0$ completely entangled photons.
Purity can be defined as the inverse of the Schmidt number K [27]. Let us consider a state $|\Psi\rangle$ identifying a composite system whose Hilbert space is $\mathcal{H} = \mathcal{H}_u \otimes \mathcal{H}_v$, with $\mathcal{H}_{u/v}$ Hilbert spaces of the subsystems that compose $|\Psi\rangle$. Introducing the orthonormal basis $\{|u_i\rangle\}$ and $\{|v_i\rangle\}$, respectively for the two spaces $\mathcal{H}_u$ and $\mathcal{H}_v$, then if $|\Psi\rangle$ is a pure state of $\mathcal{H}$, one can write

$$|\Psi\rangle = \sum_i \sqrt{\lambda_i}\,|u_i\rangle \otimes |v_i\rangle\,. \tag{2.8}$$

This is called Schmidt decomposition, where $|u_i\rangle$ and $|v_i\rangle$ are the Schmidt modes and the λ_i are said Schmidt coefficients: for these coefficients applies the relation $\sum_i \lambda_i = 1$. $|\Psi\rangle$ could represent a two-photon state and each subsystem of $|\Psi\rangle$, i.e. each single-photon state, is related to one and only one Schmidt mode.

The degree of factorizability can be inferred looking at how many Schmidt modes are necessary to completely describe the composed system, namely looking at the Schmidt coefficients. For this reason the Schmidt number is introduced as

$$K = \frac{1}{\sum_i \lambda_i^2}. \tag{2.9}$$

From this expression is clear that, for a completely factorizable two-photon state (with perfectly unentangled single photons), $K = 1$. As already stated, purity P is defined as the inverse of the Schmidt number, moreover a further relation holds between K and the second order coherence [25]:

$$K = \frac{1}{g^{(2)}(0) - 1} \quad \Longrightarrow \quad P = g^{(2)}(0) - 1. \tag{2.10}$$

For a perfectly pure single photon state a thermal statistics is expected [28], thus yielding a super-Poissonian behaviour of the light; a maximally entangled photon pair, instead, is characterized by unit second order coherence.
As a consequence maximum and minimum purity are achieved when $g^{(2)} = 2$ and $g^{(2)} = 1$, respectively.

Eq. (2.10) is of essential importance from an experimental point of view, in fact, the measurement of the second order coherence can be carried out through the HBT experiment explained in the previous section. In principle, in order to inspect the single mode character of the emitted photon, both the idler and signal beams could be used, as long as one is taken without any heralding from the other (Fig. 2.5). For sake of notation, this second order coherence is called *unheralded*.

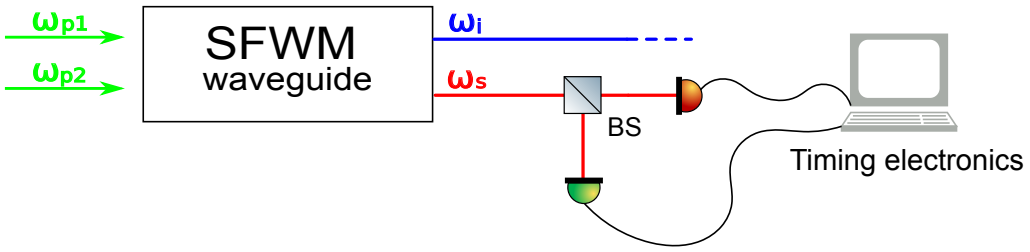

Figure 2.5: Setup for the unheralded second order coherence measurement. In principle the HBT interferometer could be used indifferently on any of the two output beams of the waveguide.

For an ideal single pulsed source, the expected shape of the $g^{(2)}$ exhibits a peak at $\Delta t = 0$, which corresponds to the coincidences within the same pulse. The peaks for non-zero delay arise, instead, because of the correlated detection of subsequent or precedent pulses.

2.2.2 Joint spectral intensity

As mentioned in Section 1.2.1, spontaneous FWM exploits the quantum vacuum fluctuations to seed the conversion of the pump photons into the signal-

idler pair. In the case of SFWM in a waveguide, the co-polarised two-photon output state can be written as [29]

$$|II\rangle \sim \iint \mathrm{d}\omega_s \, \mathrm{d}\omega_i F(\omega_s, \omega_i) \hat{a}_s^\dagger(\omega_s) \hat{a}_i^\dagger(\omega_i) |0\rangle_s |0\rangle_i , \tag{2.11}$$

where the notation of the single photon state is $|\omega\rangle_q \equiv |1\rangle_{q\omega} = \hat{a}_q^\dagger(\omega)|0\rangle$, for a photon with frequency ω in the q-th mode. The normalized biphoton function F, or joint spectral amplitude (JSA), is a function that provides information on the bandwidths of the photons involved in the non linear process. Once defined $\alpha(\omega)$, the complex amplitude of the pump spectrum centered at ω_p, the JSA can be expressed as

$$F(\omega_s, \omega_i) = \int_{-\infty}^{+\infty} \mathrm{d}\omega \alpha(\omega) \alpha(\omega_s + \omega_i - \omega) \phi(\omega_s, \omega_i, \omega), \tag{2.12}$$

where

$$\phi(\omega_s, \omega_i, \omega) = \exp\left(\frac{i\Delta\beta L}{2}\right) \mathrm{sinc}\left(\frac{\Delta\beta L}{2}\right) \tag{2.13}$$

is the phase matching function. More suitable than the JSA, is the joint spectral intensity (JSI), which is its modulus square: this quantity, measurable from the field intensity, is useful in order to estimate the degree of correlation between the signal and idler photons. From Eq. (2.12) it is clear that the JSA (and as a consequence the JSI), takes into account all the frequencies of the waves involved in the SFWM, thus allowing to determine the spectral distribution associated to one output, once the frequency of the other is given.
Once again a Schmidt decomposition can be made for the JSA, in order to quantify the degree of correlation, and so the purity of the system. For single mode emission the JSA is completely factorizable as the product of two functions; if correlations are present, it is not.
Since the measurable value is the spectral intensity, a lower bound for the true Schmidt number is calculated by considering just a singular value decomposition of the square root of the JSI.
In fact, since the modulus square of the JSA is taken, all the information on the joint spectral phase is lost.

As shown in Fig. 2.6 the joint spectral intensity ranges from a circular shape, that is the case in which the two-photon system is in a separable state, to a thin line, in the case of maximum correlation.
From an experimental point of view, it is possible to approach the single mode emission by spectral filtering. The intuitive concept is to select only certain Schmidt modes by removing the unwanted frequency modes via band pass filters. This process, however has to face the drawback given by the loss of the filtered photons, that cause a serious decrease in brightness and heralding efficiency of the source.
For these reasons, a more preferable approach is to tailor the phase matching and pump profiles, exploiting Eq. (2.12), in order to directly engineer a JSA that is intrinsically uncorrelated.

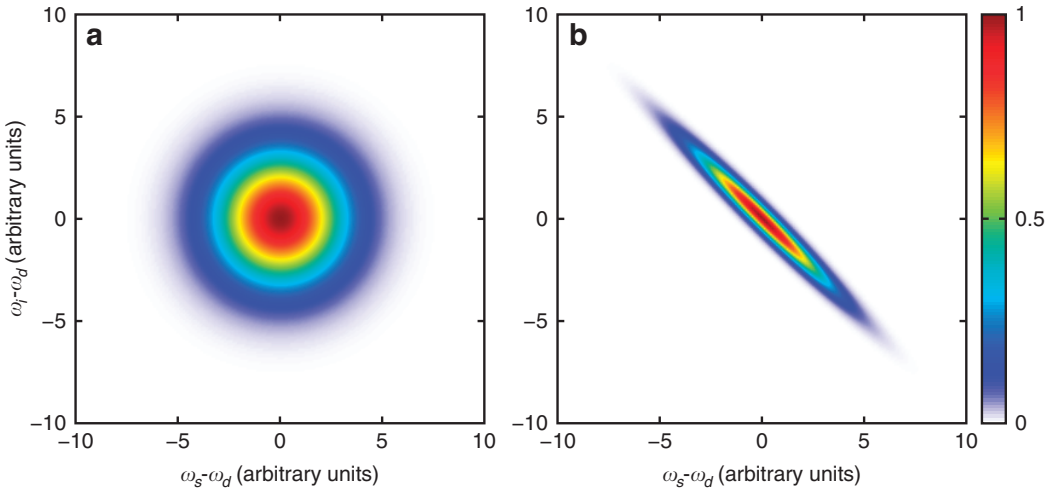

Figure 2.6: Normalised joint spectral intensity for frequency-uncorrelated (a) and frequency-correlated (b) signal and idler photons. The axes, in arbitrary units, represent the frequency shift of the generated photons with respect to the pump $\omega_d \equiv \omega_p$. Reprinted from [20].

2.2.3 Antibunching

The unheralded second order coherence, introduced in Section 2.2.1, has been shown to characterize a super-Poissonian behaviour for the isolated signal or idler beams. It has already been anticipated, however, that when the heralding process is applied the $g^{(2)}$ exhibits the antibunching dip peculiar of sub-Poissonian light. In a sense, heralding can be seen as a procedure to kill the probability of detecting zero signal photons $P(0)$.
The *heralded* second order coherence $g_h^{(2)}$ is then naturally defined as the self correlation of the signal beam triggered by the detection of its twin idler. In order to get an experimental estimate, it is again made use of the HBT interferometer on the signal beam, but with the fundamental difference that a detector on the idler arm is added to the timing electronics. A schematization of this set-up is shown in Fig. 2.7.

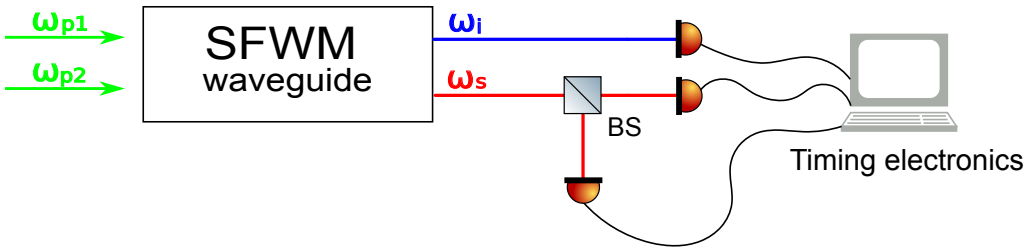

Figure 2.7: Setup for the heralded second order coherence measurement. The source is based on a SFWM process in a waveguide.

Since the detection of coincidences in the signal arm is triggered only by the detection of the herald, the $g_h^{(2)}$ is said to be conditioned by the idler. Using the destruction and creation operators notation, this function can be written

as [25]

$$g_h^{(2)}(t_1, t_2|t_i) = \frac{\langle \hat{a}_i^\dagger \hat{a}_1^\dagger \hat{a}_2^\dagger \hat{a}_2 \hat{a}_1 \hat{a}_i \rangle}{\langle \hat{a}_i^\dagger \hat{a}_1^\dagger \hat{a}_1 \hat{a}_i \rangle \langle \hat{a}_i^\dagger \hat{a}_2^\dagger \hat{a}_2 \hat{a}_i \rangle} \langle \hat{a}_i^\dagger \hat{a}_i \rangle, \tag{2.14}$$

where for sake of simplicity the temporal dependence of the operators is omitted and the subscripts 1, 2 and i identify, respectively, the two signal detectors and the idler. Considering a zero delay between the detection of the idler and the signal of detector 1, which is typically the case in heralded sources measurements, the correlation becomes a function only of $\Delta t = t_2 - t$, with $t \equiv t_1 = t_i$.

2.2.4 Heralding efficiency

As already pointed out discussing the JSI, a high purity is often achieved by heavy filtering of the beam sources. The drawback is the irredeemable loss of photons, preventing an efficient heralding procedure. To quantify the quality of the heralding procedure considering the associated losses, the heralding efficiency is introduced: this parameter is the probability to detect the heralded photon, given the detection of the herald. In the definition of heralding efficiency is necessary a term that accounts for the imperfect detection of photons performed by the real-world detectors: the detection efficiency η_d. Identifying the herald with the idler, it is possible to write

$$\eta_H^s = \frac{R_{si}}{R_i \eta_d^s}, \tag{2.15}$$

where R_{si} and R_i are the signal-idler coincidences rate and the detection rate of the idler, respectively.
Very often the heralding efficiency is affected by losses in the instrumentation used to characterize the source or by limited fabrication quality of the chip. In order to get rid of these losses and focus on the source design performance, the intrinsic heralding efficiency is introduced. By denoting with T_s the transmission of the signal by the photon source, then the intrinsic heralding efficiency can be expressed as

$$\eta_I = \frac{\eta_H^s}{T_s}. \tag{2.16}$$

2.2.5 Coincidence to accidental ratio

In an effort to characterize a heralded photon source, it is useful to have a parameter which quantifies the overall coincidence detection efficiency between signal and idler. Analogously to the signal to noise ratio in a generic photon source, but extending the concept to the pair generation and coincidence detection, it is introduced the coincidence to accidental ratio (CAR).
Only the coincidences occurring between signal and idler that belong to the same initial pair are the actual coincidences that characterize the temporal

correlation of the emitted photons. On the contrary, the coincidences of signal and idler photons of distinct pairs are indicated as accidental coincidences. Accidental coincidences occur when a signal/idler photon is lost and a simultaneous detection with an idler/signal of a different pair is measured. An optimal source of photon pairs would be characterized by a rate of "good" coincidences R_{si} much greater than the rate of accidental ones R_{acc}. Consequently, for an ideal source the CAR, defined as

$$CAR = \frac{R_{si} - R_{acc}}{R_{acc}}, \tag{2.17}$$

would approach infinity. From an experimental point of view, the measurement of this parameter is carried out by connecting the timing electronics to the idler and signal detectors, as shown in Fig. 2.8.

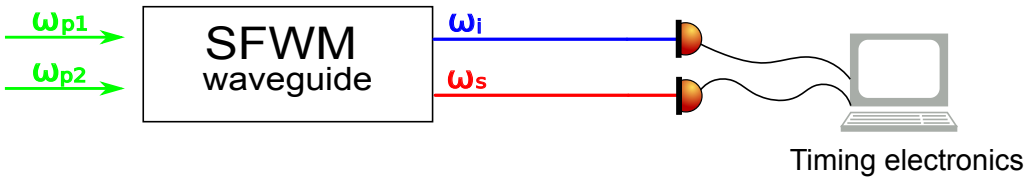

Figure 2.8: Setup for the coincidence to accidental ratio measurement. The source is based on a SFWM process in a waveguide.

2.2.6 Other parameters

Another useful parameter for the characterization of light sources is the brightness B, that is the emission rate of single photons. The brightness of a pulsed light source can be defined as the probability of detecting a single photon every laser pump pulse [21]. This parameter is used for both deterministic and probabilistic photon sources. For the latter the probability of emission scales with the pump power P_p. In particular, for four wave mixing processes $P(1) \propto P_p^2$ and $P(2) \propto P_p^4$ [8]. This means that the emission rate of multiphoton states (thus the brightness) can be modified applying the proper power.

As mentioned before, several quantum information protocols, for instance where qubits interactions need to occur in order to perform logic operations, require high visibility interference between single photons [26]. This feature demands photons which are indistinguishable in terms of energy, bandwidth and polarization. Due to the phase matching issue already discussed, the spectral emission properties of a source are challenging to control when compared to the polarization and momentum of the output photons, that are more easily tractable.
For these reasons the indistinguishability and quantum interference are often taken into account when describing the main features of a photon source.

2.3 Chip design and experimental set-up

The vision of an integrated quantum photonic chip, capable to fully process the quantum states of light, requires three main components: the source, the manipulation circuit and the detector of the quantum states. While the manipulation part has reached noticeable advancements [20], a valid solution for the integration of the other components is still missing. As for the source, it is of great interest the on-chip production of single photons performed through heralded single photon generation.
The access to on-chip nonlinear phenomena is possible thanks to the waveguide technology (Sec. 1.2), which guarantees a high optical intensity, thus lowering the power requirements. The aforementioned advantages in the use of Silicon with respect to other materials, in addition to its high nonlinear index, make this material the best choice for nonlinear integrated applications. These applications range from quantum light generation to wavelength conversion, from sensing and metrology to all kinds of signal processing. As for quantum applications, it has been demonstrated that one can use nonlinear processes, such as FWM, as a source of correlated photon pairs [30]. Among the other applications, the opportunity to generate quantum light in the mid infrared (from $2\,\mu$m to $20\,\mu$m), is appealing for applications in quantum sensing, such as the high-sensitivity probing of gas molecules, or in quantum communications, since several transparent windows of the atmosphere are found in the mid infrared (MIR), thus allowing low loss free space data exchange.
In this section is initially presented a chip implementing a heralded single photon source based on IFWM on a SOI multimode waveguide. Its characterization is reported in Chap. 3. The idler photon, used as herald, is generated at $1.26\,\mu$m, while the signal photon, the heralded one, is generated in the MIR at $2.011\,\mu$m. Having the photon pair generated at these wavelengths is a non-negligible advantage: in fact, standard InGaAs single-photon avalanche diode (SPAD) are highly efficient at the idler bandwidth and the signal photon is still below the absorption edge of silicon dioxide. In the last part of the section the experimental setup for the source characterization is described.

2.3.1 Integrated chip

The third order nonlinear process used to generate the correlated photon pair is intermodal SFWM. It is performed in a multimode silicon rib waveguide, whose cross section and measures are sketched in Fig. 2.9. The polarization used is the transverse electric (TE), in fact the rib geometry chosen does not allow TM polarization propagation. The intermodal combination used is the 1221TE: one pump photon on TE0 mode, the other on TE1 mode, while the signal and idler are on TE1 and TE0 modes respectively.
In Fig. 2.10 the chip scheme is shown. At the beginning, the pump is splitted via a 3dB directional coupler (A): in this way half of the initial power is coupled on the first TE mode on arm 2, while the other half is propagating along arm 1.

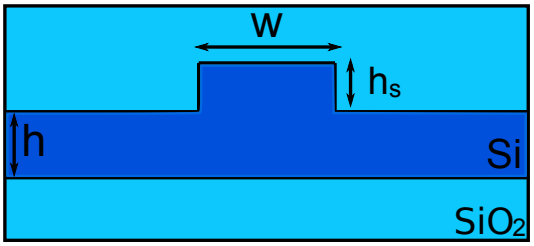

Figure 2.9: Cross-section of the SOI rib geometry of the waveguide. The nominal width of the waveguide used is $w = 1.95\,\mu$m, the height of the strip is $h_s = 190\,$nm and the height of the slab $h = 300\,$nm. The material used for the core is silicon, while the cladding and substrate are made of silica.

An asymmetric directional coupler (ADC) is then used as mode converter (B), in particular the power of the first order mode coupled in arm 1 is coupled on the second TE order mode of the waveguide 2.

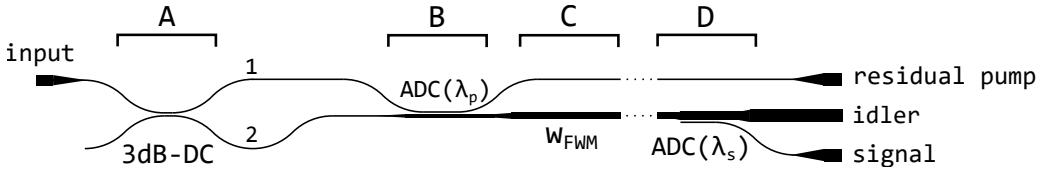

Figure 2.10: Chip scheme. The input and output ports are tapered to a width of 3.7 μm, in order to maximize the coupling with the tapered lensed fibers used to inject and extract the light.

The ADC, with respect to the standard directional coupler, exploits two different widths of the waveguides: when a single mode waveguide is placed close to a multimode waveguide, it is possible to excite selectively one of the supported different order modes.
Now, on the the same waveguide 2, half of the pump power is travelling on the first TE order mode, while the other half excites the second TE order mode. By modifying the geometry of this waveguide is reached the width w_{FWM} necessary for the correct phase matching of the FWM process (C). At the end (D) another ADC is used to separate the signal wavelength from the idler: idler and signal are in this way separated on-chip, without the necessity of further filtering.

2.3.2 Measurement set-up

The experimental setup used for the heralded single photon source is sketched in Fig. 2.11.

A 1.55 μm pulsed laser pump is used, with a 40 ps pulse duration and 80 MHz repetition rate. The pump is coupled into the chip via a lensed fiber. Signal and idler are extracted from the chip with two tapered lensed fibers. The idler is sent through a low pass filter at 1350 nm and then detected via a InGaAs detector. The signal, after going through a 1900 nm long pass filter, is sent to the up-conversion system. Here, in the PPLN crystal up-converter,

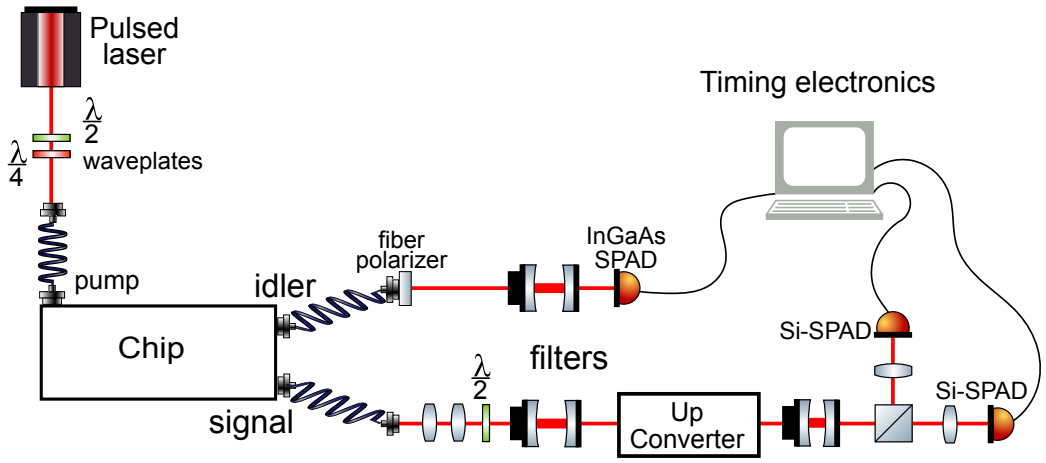

Figure 2.11: Sketch of the setup in the case of the heralding experiment. For the purity and Car measurements the timing electronics is connected accordingly to Fig. 2.5 and 2.8, respectively.

the 2 μm signal is mixed with a pump photon at 1064 nm to generate one at 695 nm via the second order nonlinear process of sum frequency generation. In the case of a HBT experiment, the visible photon subsequently goes through the beam splitter and two silicon SPADs count the transmitted or reflected photons. For other type of measurements, e.g. the CAR, the up-converted light is directly detected by a Si-SPAD. In the sketch, the timing electronics is connected for a HBT experiment, but depending on which kind of measurement is performed, the different SPADs are connected according to Fig. 2.5 or 2.8. As for the coincidence electronics, a Time Tagger has been used. This device is a time-to-digital converter and logic analyzer able to perform Time-Correlated Single-Photon Counting (TCSPC), start-stop and cross-correlations measurements.

Chapter 3

Characterization of a heralded single photon source

In this chapter are presented the results of the measurements performed in order to characterize the heralded single photon source described in Section 2.3.

3.1 CAR measurement

For the coincidence to accidental ratio experimental measurement, in the pulsed source case, instead of the coincidence rate of Eq. (2.17), it is possible to use the number of coincidence counts $N(t)$. It is sufficient to notice that the number of accidental occurrences is just the number of the delayed signal-idler coincidences $N(\Delta t)$:

$$CAR = \frac{N_{si} - N_{acc}}{N_{acc}} = \frac{N_{si}(0)}{N_{si}(\Delta t > 0)} - 1, \tag{3.1}$$

that, using the results of Sec. 3.2, can also be written as $CAR = g^{(2)}_{si} - 1$.
As for the measurement procedure, even if the laser pump duration is nominally 40 ps, $N_{si}(\Delta t)$ has been measured integrating the coincidence counts under a bin width of 1 ns, in order to account for the jitter of detectors and electronics.
For sake of comparison with other sources, since the up-converter noise is not-negligible at all, it is given both a raw CAR value and a noise corrected one.
In order to perform this correction, the average noise counts falling between two subsequent pump pulses are subtracted to all the bins containing the signal photons.
In Fig. 3.2 is reported, as an example, the measured histogram for a 15.7 mW pump power. The bins are centered at multiple pump periods; the raw counts are in blue, while the noise corrected ones in red.

As one can notice from Fig. 3.1 and 3.2, the acquisition time seems to be long enough for a proper CAR estimation. In fact the bin height results almost the same for all the delayed side peaks. In the inset of Fig. 3.1, an example of

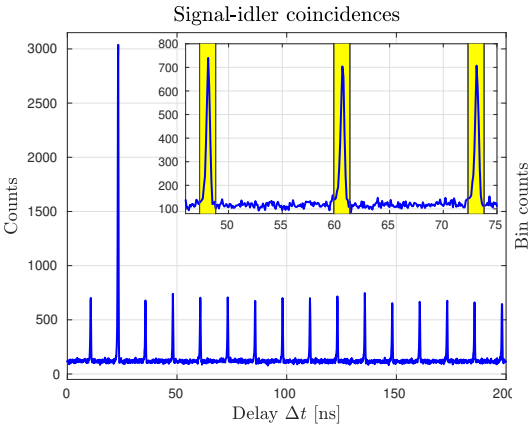

Figure 3.1: Example of signal-idler counts as a function of the time delay for $P_p = 15.7\,\text{mW}$. In the inset the 1 ns integration bin is represented by the yellow bands.

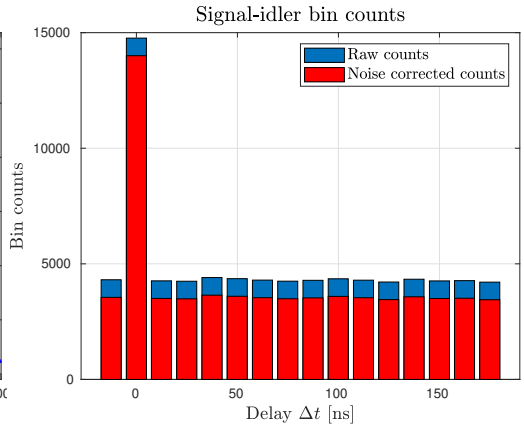

Figure 3.2: Example of signal-idler bin counts for $P_p = 15.7\,\text{mW}$. The ratio between the zero-delay peak and the average of the side bars gives the CAR.

the coincidence counts is present, where the 1 ns integration bin is represented by the yellow bands.
The CAR, with and without noise correction, is calculated for 10 different pump power values (Fig. 3.3). As the power decreases, the CAR value, both raw

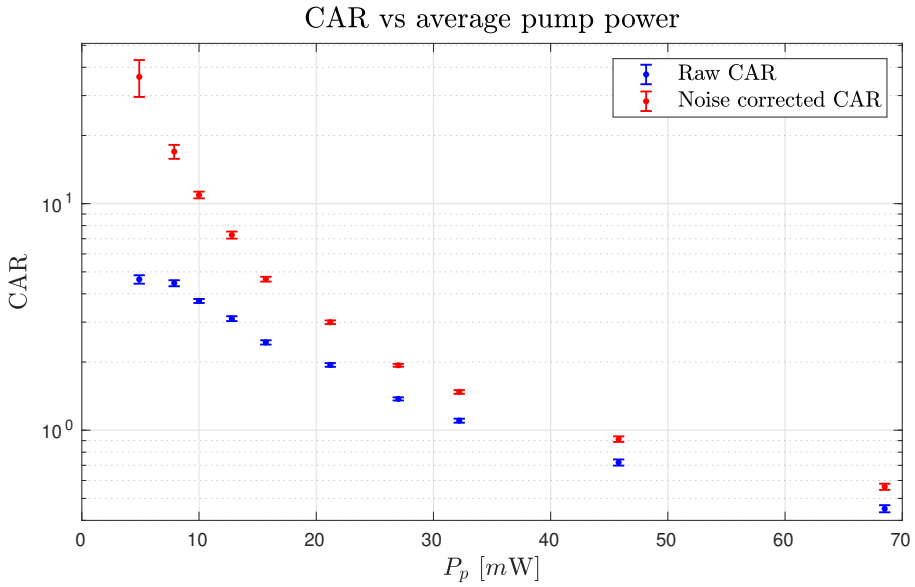

Figure 3.3: CAR as a function of the average pump power. In blue the raw values and in orange the noise corrected ones.

and corrected, becomes higher. That is an expected behaviour, since as previously stated, the dependence of multipair generation probability on the average pump power is $P(1) \propto P_p^2$ and $P(2) \propto P_p^4$.
The maximum value for the non corrected CAR is 4.6(2), while the maximum corrected CAR is 36(5).

3.2 Purity estimation

The relation between the purity of a heralded single photon P and the zero-delay second order coherence has already been outlined in Sec. 2.2.1. From an experimental point of view the $g^{(2)}$ can be expressed as a function of the probability detection of coincidences at a fixed delay, previously called Δt, as

$$g^{(2)}(\Delta t) = \frac{P_{ss}(\Delta t)}{P_s(t)P_s(\Delta t)} \tag{3.2}$$

where the subscripts indicate that the measured beam is the signal. $P_{ss}(\Delta t)$ identifies the probability of coincidences detection with a Δt between the two HBT channels, and $P_s \equiv P_s(\Delta t) = P_s(t)$ is the detection probability of a single detector, which depends neither by time, nor the detector.
From its definition in Eq. (2.3), it can be seen that the numerator of the $g^{(2)}$, for each Δt, measures the number of coincidences given by the delayed detection events in the two arms of the interferometer. Subsequently the number of coincidences are averaged over all the ensemble coincidence events.
In the case of a pulsed laser, the ensemble average is simply the average on the N_p pump pulses used for the measurement. The total number of coincidences is then $N_{ss}(\Delta t) = P_{ss}(\Delta t)N_p$. It is possible to exploit the fact that, when the Δt between coincidence counts is longer than the pulse duration, the two detectors detections are independent events:

$$P_{ss}(\Delta t > 0) = P_s(t)P_s(\Delta t) = P_s P_s \tag{3.3}$$

As a consequence, taking the number of zero delay coincidences over the number of subsequent coincidence events yields, using Eq. (3.2):

$$\frac{N_{ss}(0)}{N_{ss}(\Delta t > 0)} = \frac{P_{ss}(0)N_p}{P_{ss}(\Delta t > 0)N_p} = \frac{P_{ss}(0)}{P_s P_s} = g^{(2)}(0). \tag{3.4}$$

Clearly, also the unheralded second order coherence for non-zero delay can be calculated, but in that case also the numerator of Eq. (3.4), would be factorizable, yielding unit $g^{(2)}$.

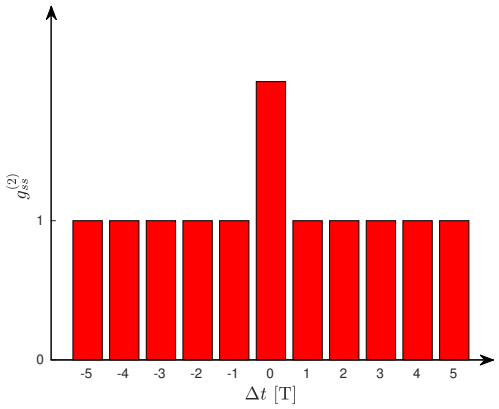

Figure 3.4: Expected $g^{(2)}$ as a function of the time delay for a pulsed source: the pump is pulsed with repetition rate $1/T$.

This fact can be seen in Fig. 3.4, where is represented the expected $g^{(2)}$ as a function of time.
The $g^{(2)}$ measurement has been carried out exactly like the CAR, thus by integrating over a defined bin width, with and without noise correction. In Fig. 3.6 is reported, as an example, the measured histogram for a 25.04 mW pump power. From both Fig. 3.5 and 3.6, is clear that longer acquisition times are

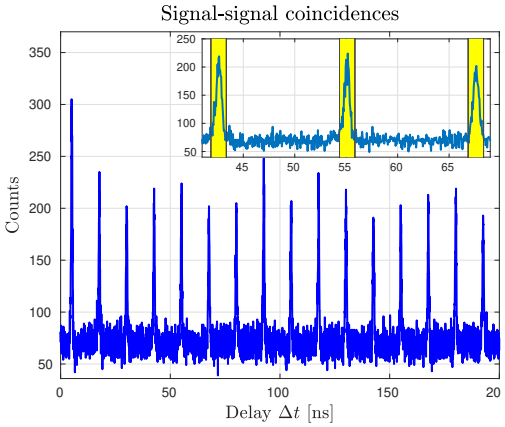

Figure 3.5: Example of counts as a function of the time delay for $P_p = 25.04\,\text{mW}$. In the inset the 1 ns integration bin is represented by the yellow bands.

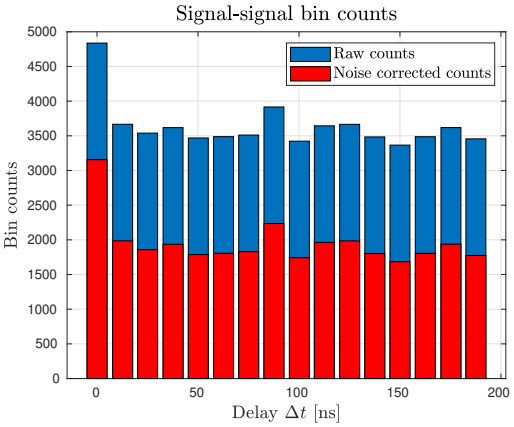

Figure 3.6: Example of signal-signal bin counts for $P_p = 25.04\,\text{mW}$. The ratio between the zero-delay peak and the average of the side bars gives the $g^{(2)}$.

required for a better $g^{(2)}$ estimation: in fact the delayed peaks heights are not the same, as instead it should be for a measure carried on long enough. Still, the unheralded $g^{(2)}$ has been measured for various input powers, as shown in Fig. 3.7, for the signal photon in the MIR. It is noteworthy that a lower power is

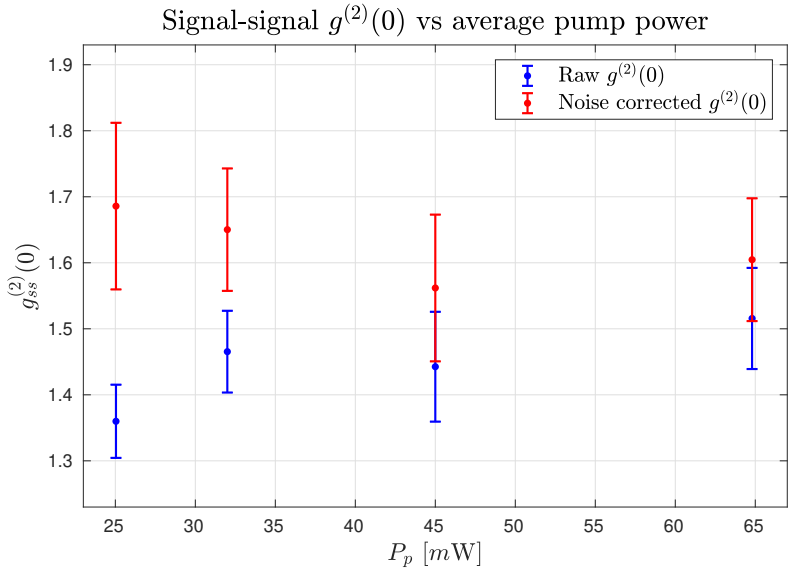

Figure 3.7: Unheralded $g^{(2)}$ as a function of the average pump power. In blue the raw values and in orange the noise corrected ones.

again beneficial, since a reduced multipair generation increases the unheralded

$g^{(2)}$. The maximum measured purity of the single photon state, calculated as $P = 1 - g^{(2)}(0)$, is found for the minimum power and results 0.68(13).

3.3 Antibunching dip

The final measure performed is the heralded second order coherence. Starting from the expression of the conditioned second order coherence in Eq. (2.14) and developing the concepts of Sec. 3.2, one can write the heralded $g^{(2)}$ as a function of the number of coincidences as

$$g_h^{(2)}(\Delta t) = \frac{N_{12i}(\Delta t)}{N_{1i}(t)N_{2i}(\Delta t)} N_i(t), \tag{3.5}$$

where N_{12i} indicates the three-fold coincidences between the idler and the arms 1 and 2 of the HBT interferometer; the two-fold coincidences counts between only one signal beam and the herald are, instead, N_{1i} and N_{2i}; finally N_i is the number of idler detections. Once again, in the case of a pulsed source the probabilities are factorizable, yielding a unit second order coherence when $\Delta t > 0$.
As a consequence, for a sub-Poissonian pulsed light, the $g_h^{(2)}$ expected profile is the one sketched in Fig. 3.8. According to Eq. (3.5) in principle, three-fold,

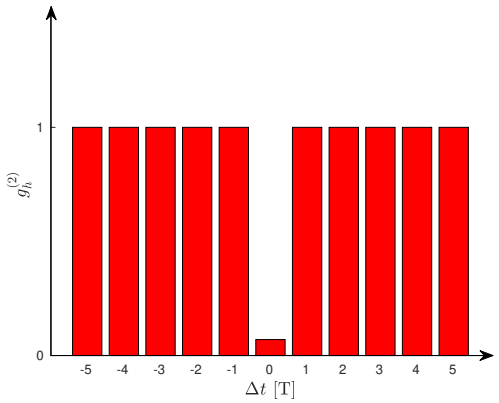

Figure 3.8: Expected $g_h^{(2)}$ for a sub-Poissonian pulsed light as a function of the time delay. The pump is pulsed with repetition rate $1/T$.

two-fold and single idler coincidences should be measured simultaneously in order to get the actual shape of the second order coherence. But, since the quantity of interest is the zero-delay $g_h^{(2)}$, keeping in mind that $P = P(t_2) = P(t)$ it is possible to write

$$\begin{aligned} g_h^{(2)}(0) &= \frac{N_{12i}(0)}{N_{1i}(t_2)N_{2i}(0)} N_i(t_2) = \frac{P_{12i}(0)N_p}{P_{2i}(0)N_p} \frac{P_i N_p}{P_{1i}N_p} = \frac{P_{12i}(0)}{P_{2i}(0)} \frac{P_i}{P_1 P_i} \frac{P_2}{P_2} \\ &= \frac{P_{12i}(0)}{P_{2i}(0)} \frac{P_{2i}}{P_{12i}} = \frac{N_{12i}(0)}{N_{2i}(0)} \frac{N_{2i}(\Delta t > 0)}{N_{12i}(\Delta t > 0)} = \frac{N_3(0)}{N_3(\Delta t > 0)}, \end{aligned} \tag{3.6}$$

where $N_3(\Delta t)$ is defined as the three-fold and two-fold ratio $\frac{N_{12i}(\Delta t)}{N_{2i}(\Delta t)}$. Eq. (3.6) then gives a pragmatical result that allows to measure the antibunching as the ratio between the non-delayed and the delayed N_3 counts.
The analysis of the heralded $g^{(2)}$ has been conducted analogously to the unheralded one. In Fig. 3.9 and 3.10 are present the bin counts for both the three-fold and two-fold coincidences, measured for $P_p = 20.4\,\text{mW}$.

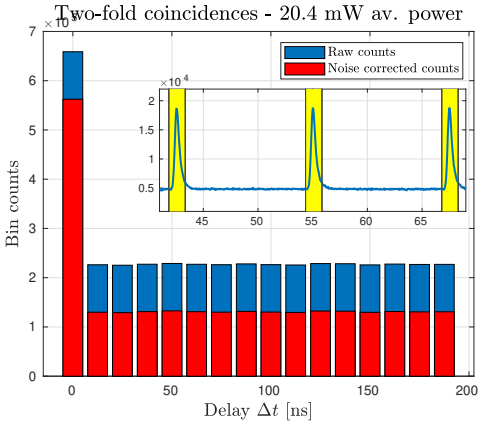

Figure 3.9: Example of the two-fold bin counts as a function of the delay Δt, for $P_p = 20.4\,\text{mW}$.

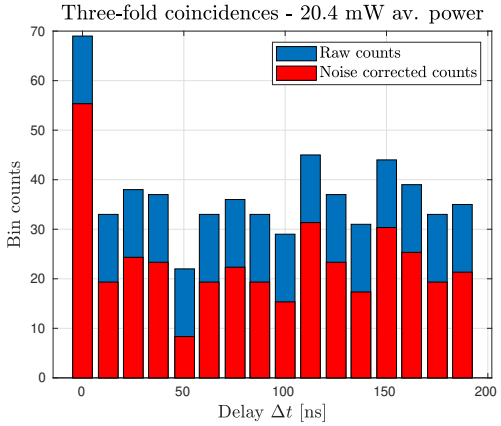

Figure 3.10: Example of the three-fold bin counts as a function of the delay Δt, for $P_p = 20.4\,\text{mW}$.

If, on one hand, the two-fold coincidences do not reveal any acquisition time problem whatsoever, on the other hand it is clear that the integration time is not enough for the three fold. The side peaks are indeed all different, due to the fact that a proper acquisition time would be prohibitive with the setup used. Nonetheless, the measurement of the heralded second order coherence has been performed for different pump powers. The results, for the noise corrected

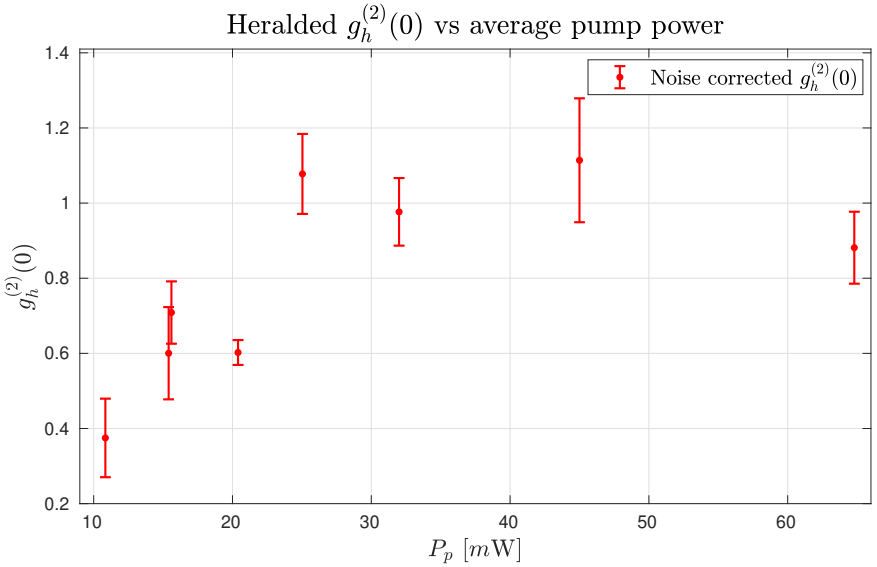

Figure 3.11: Heralded $g^{(2)}$ as a function of the average pump power.

values, can be seen in Fig. 3.11. Manifestly, due to the higher probability of multipair emission the $g_h^{(2)}$ increases as the average pump power is higher. From these measurements it is clear the presence of antibunching behaviour, especially for the lower values of P_p. However, as explained in Sec. 2.1.1, a true single photon emission behaviour can be claimed only with a conditioned second order coherence below 0.5. Thus, only for the minimum power value used, we can assert to have single photon emission, in particular the minimum measured value of $g_h^{(2)}$ is 0.37(9).

Conclusions

A quantum device able to successfully encode and manipulate information on a large scale would provide unprecedented computational power and unconditionally secure communication. In this regard, the use of single photons as qubits is a particularly appealing concept. The photons low decoherence and inherent low-loss transmission are key features required for quantum computing and quantum communication applications. In this scheme, integrated single photon sources are fundamental ingredients in the development of reliable quantum architectures.
Within the photonics framework, the use of silicon technology has not equals in terms of fabrication reliability and footprint. In chapter 1 have been discussed the advantages of the use of silicon and its dioxide for the optical waveguides fabrication. Moreover, the formation and subsequent propagation of waveguide modes in a multimode waveguide has been presented. A brief overview of nonlinear processes has been reported and, in view of a single photon source implementation, particular focus has been given to four wave mixing. While intramodal FWM has a limited generation bandwidth, and cannot access the mid infrared part of the spectrum, intermodal FWM enables larger spectral translations. IFWM thus provides a suitable mechanism for the implementation of heralded single photon sources with a large detuning between the generated idler and signal. This is the topic of chapter 2, where the basics of single photon sources are introduced. Here, the focus is on the heralded sources, where the detection of one photon heralds the creation of the other. The major experimental parameters and metrics for the characterization of heralded single photon sources are subsequently provided.
Ultimately, a on-chip heralded single photon source exploiting intermodal FWM is presented. After a brief description of the chip scheme, the measurement setup used for its characterization is outlined.
In the third chapter of this thesis, I conducted an analysis of the measurements performed in order to estimate the main experimental parameters of the source. Due to the significant noise, mainly generated by the up-converter, a correction procedure had to be carried on. The generation of single photons at 2.011 μm heralded by the idler at 1.26 μm have been demonstrated. In fact, a minimum heralded second order coherence of 0.37(9) is measured. A maximum purity of 0.68(13) and a maximum CAR of 36(5) are obtained. These

parameters do not exceed the results of other sources, such as ring resonators [31], but the purpose of the experiment was to show the possibility to have a single photon source with a large spectral conversion exploiting IFWM, rather than the demonstration of a high purity source. These results are promising for the developing of mid infrared photonics, where a viable integrated source of light is still missing. Integrated quantum devices in the MIR wavelength, would provide a new powerful tool for the implementation of free space communications and quantum sensing.

Bibliography

[1] R. A. Soref, "Silicon-based optoelectronics," *Proceedings of the IEEE*, vol. 81, 1993.

[2] G. K. Celler et al., "Frontiers of silicon-on-insulator," *Journal of Applied Physics*, vol. 93, 2003.

[3] C. Grivas, "Optically pumped planar waveguide lasers, part i: Fundamentals and fabrication techniques," *Progress in Quantum Electronics*, vol. 35, 2011.

[4] M. C. T. Bahaa E. A. Saleh, *Fundamentals of photonics*. Wiley series in pure and applied optics, Wiley, 1st ed., 1991.

[5] S. Signorini, "Intermodal four wave mixing for heralded single photon sources in silicon," *Phd Thesis. University of Trento*, 2019.

[6] A. De Rossi et al., "Measuring propagation loss in a multimode semiconductor waveguide," *Journal of Applied Physics*, vol. 97, 2005.

[7] S. Signorini et al., "Intermodal four-wave mixing in silicon waveguides," *Photonics Research*, vol. 6, 08 2018.

[8] M. Borghi et al., "Nonlinear silicon photonics," *Journal of Optics (IOPscience)*, 06 2017.

[9] J. Leuthold et al., "Nonlinear silicon photonics," *Nature Photonics*, vol. 4, 2010.

[10] R. W. Boyd, *Nonlinear optics*. Academic Press, 3 ed., 2008.

[11] J. W. Silverstone et al., "On-chip quantum interference between silicon photon-pair sources," *Nature Photonics*, vol. 8, 12 2013.

[12] A. Anchal et al., Pascal, "Frequency-shift free optical phase conjugation using counter-propagating dual pump four-wave mixing in fiber," *Journal of Optics (IOPscience)*, vol. 18, 03 2016.

[13] K. Wang et al., "Four-wave-mixing based silicon integrated optical isolator with dynamic non-reciprocity," *IEEE Photonics Technology Letters*, 2016.

[14] M. A. Foster et al., "Broad-band optical parametric gain on a silicon photonic chip," *Nature*, vol. 441, 2006.

[15] I. Cerutti et al., "Engineering of closely packed silicon-on-isolator waveguide arrays for mode division multiplexing applications," *Journal of the Optical Society of America B*, vol. 34, 02 2017.

[16] E. Knill et al., "A scheme for efficient quantum computation with linear optics," *Nature*, vol. 409, 01 2001.

[17] J. B. Spring et al., "Boson sampling on a photonic chip," *Science*, vol. 339, 02 2013.

[18] H. J. Briegel et al., "Quantum repeaters: The role of imperfect local operations in quantum communication," *Physical Review Letters*, vol. 81, 1998.

[19] B. Schumacher, "Quantum coding," *Physical Review A*, vol. 51, 1995.

[20] L. Caspani et al., "Integrated sources of photon quantum states based on nonlinear optics," *Light: Science and Applications*, vol. 6, 11 2017.

[21] M. D. Eisaman et al., "Invited review article: Single-photon sources and detectors," *Review of Scientific Instruments*, vol. 82, 2011.

[22] X. L. Chu et al., "A single molecule as a high-fidelity photon gun for producing intensity-squeezed light," *Nature Photonics*, vol. 11, 12 2016.

[23] L. Dusanowski et al., "Near-unity indistinguishability single photon source for large-scale integrated quantum optics," *Physical Review Letters*, vol. 122, 5 2019.

[24] A. Kuhn et al, "Deterministic single-photon source for distributed quantum networking," *Physical Review Letters*, vol. 89, 7 2002.

[25] A. Migdall, S. V. Polyakov, J. Fan, J. C. Bienfang, *Single-Photon Generation and Detection: Physics and Applications*. Experimental Methods in the Physical Sciences 45, Academic Press, 1 ed., 2013.

[26] J. Beugnon et al., "Quantum interference between two single photons emitted by independently trapped atoms," *Nature*, vol. 440, 2006.

[27] R. Loudon, *The Quantum Theory of Light, 3rd ed. (Oxford Science Publications)*. Oxford University Press, USA, 3 ed., 2000.

[28] A. K. Ekert, "Correlations and squeezing of two-mode oscillations," *American Journal of Physics*, vol. 57, 1989.

[29] I. Jizan et al., "Bi-photon spectral correlation measurements from a silicon nanowire in the quantum and classical regimes," *Scientific Reports*, vol. 5, 12 2015.

[30] A. R. McMillan et al., "Narrowband high-fidelity all-fibre source of heralded single photons at 1570 nm," *Optics Express*, vol. 17, 2009.

[31] M. Chaoxuan et al., "Silicon photonic entangled photon-pair and heralded single photon generation with $car > 12000$ and $g^{(2)}(0) < 0006$," *Optics Express*, vol. 25, 12 2017.

[32] S. Paesani et al., "Near-ideal spontaneous photon sources in silicon quantum photonics," *Nature Communications*, vol. 11, 12 2020.

[33] C. Santori, "Quantum optics: A brighter source of single photons," *Nature Photonics*, vol. 1, 2007.